Article:
Jones, R.A., Cooper, F., Kelly, G. et al. (2024) Zebrafish reveal new roles for Fam83f in hatching and the DNA damage-mediated autophagic response. Open Biology, 14 (10). 240194. ISSN: 2046-2441

https://doi.org/10.1098/rsob.240194

OPEN BIOLOGY

royalsocietypublishing.org/journal/rsob

Research

Cite this article: Jones RA, Cooper F, Kelly G, Barry D, Renshaw MJ, Sapkota G, Smith JC. 2024 Zebrafish reveal new roles for Fam83f in hatching and the DNA damage-mediated autophagic response. *Open Biol.* **14**: 240194.
https://doi.org/10.1098/rsob.240194

Received: 11 July 2024
Accepted: 25 July 2024

Subject Areas:
developmental biology, cellular biology

Keywords:
zebrafish, Fam83f, DNA damage, autophagy, development, hatching

Author for correspondence:
Rebecca A. Jones
e-mail: rj2787@princeton.edu

Electronic supplementary material is available online at https://doi.org/10.6084/m9.figshare.c.7468066.

THE ROYAL SOCIETY PUBLISHING

Zebrafish reveal new roles for Fam83f in hatching and the DNA damage-mediated autophagic response

Rebecca A. Jones[1], Fay Cooper[2,3], Gavin Kelly[4], David Barry[4], Matthew J. Renshaw[4], Gopal Sapkota[5] and James C. Smith[4]

[1]Department of Molecular Biology, Princeton University, Princeton, NJ 08544, USA
[2]School of Biosciences, and [3]Neuroscience Institute, University of Sheffield, Sheffield S10 2TN, UK
[4]The Francis Crick Institute, 1 Midland Road, London NW1 1AT, UK
[5]MRC Protein Phosphorylation and Ubiquitylation Unit, School of Life Sciences, University of Dundee, Dow Street, Dundee DD1 5EH, UK

RAJ, 0000-0002-1530-5400; GK, 0000-0001-7219-560X; GS, 0000-0001-9931-3338; JCS, 0000-0003-2413-9392

The FAM83 (Family with sequence similarity 83) family is highly conserved in vertebrates, but little is known of the functions of these proteins beyond their association with oncogenesis. Of the family, FAM83F is of particular interest because it is the only membrane-targeted FAM83 protein. When overexpressed, FAM83F activates the canonical Wnt signalling pathway and binds to and stabilizes p53; it therefore interacts with two pathways often dysregulated in disease. Insights into gene function can often be gained by studying the roles they play during development, and here we report the generation of *fam83f* knock-out (KO) zebrafish, which we have used to study the role of Fam83f *in vivo*. We show that endogenous *fam83f* is most strongly expressed in the hatching gland of developing zebrafish embryos, and that *fam83f* KO embryos hatch earlier than their wild-type (WT) counterparts, despite developing at a comparable rate. We also demonstrate that *fam83f* KO embryos are more sensitive to ionizing radiation than WT embryos—an unexpected finding, bearing in mind the previously reported ability of FAM83F to stabilize p53. Transcriptomic analysis shows that loss of *fam83f* leads to downregulation of phosphatidylinositol-3-phosphate (PI(3)P) binding proteins and impairment of cellular degradation pathways, particularly autophagy, a crucial component of the DNA damage response. Finally, we show that Fam83f protein is itself targeted to the lysosome when overexpressed in HEK293T cells, and that this localization is dependent upon a C′ terminal signal sequence. The zebrafish lines we have generated suggest that Fam83f plays an important role in autophagic/lysosomal processes, resulting in dysregulated hatching and increased sensitivity to genotoxic stress *in vivo*.

1. Introduction

The FAM83 family is a poorly understood group of eight proteins, with members designated A–H, that is characterized by a highly conserved DUF1669 domain (domain of unknown function 1669) at the N-termini of family members [1–3]. FAM83 proteins are present in all jawed vertebrates, with no orthologues described in simpler organisms such as nematodes or *Drosophila*. There is little sequence homology outside the DUF domain, and although the DUF1669 structure is known (PDB 5LZK [4]), the structures of the highly variable carboxy-termini are not.

The primary amino acid sequences of the FAM83 family give little insight into their function. The DUF1669 domain contains a pseudo-phospholipase D (PLD) domain, but no PLD enzymatic activity has been recorded for any of the family members [5]. Until recently, most attention has been paid to the oncogenic properties of the FAM83 family in numerous cancers. Broadly speaking, the FAM83 family members are found to be overexpressed in many cancers, with some (like FAM83A) being implicated in acquired therapy resistance [6]. Although less is known about the role of FAM83F in oncogenesis compared with other family members, it is linked to oesophageal small-cell carcinoma [7], papillary thyroid cancer [8], non-small cell lung cancer [9–11] and breast and cervical cancer [12,13]; increased expression is also implicated in poor patient survival in other cancers [14]. Despite studies over the last decade increasingly associating the FAM83 family with oncogenesis, the mechanisms by which they drive tumorigenicity are largely unknown [15,16].

The FAM83 family has been associated with several signalling pathways, and members interact with many different binding partners, including c-RAF and PI3K (FAM83A [6]), RAS and cRAF (FAM83B [17]), the chromokinesin KID and dynein light chain (DYNLL1) (FAM83D [18,19]), SMAD1 and CD2AP (FAM83G [20,21]) and keratins (FAM83H [22]). Using a proteomics approach, Fulcher *et al*. [23] showed that all members of the FAM83 family bind at least one isoform of casein kinase 1 (CK1), a pleiotropic and highly conserved serine/threonine kinase involved in many cellular processes and implicated in carcinogenesis [24]. All family members bind to the CK1α isoform, and these interactions contribute to the sub-cellular localization of both proteins. This interaction with CK1α is dependent upon a F-x-x-x-F sequence motif towards the C-terminus of the DUF1669 domain of the FAM83 family proteins [23].

With respect to specific FAM83F interactors, both FAM83F and its most closely related family member, FAM83G, regulate canonical Wnt signalling through their interaction with CK1α, and when overexpressed in *Xenopus laevis* embryos, both induce a complete secondary axis [3,25]. Mutation of either of the phenylalanine residues in the F-x-x-x-F sequence motif of FAM83F renders the protein incapable of modulating the Wnt pathway [25]. FAM83F also binds to and stabilizes p53 [26], and in doing so increases its activity. FAM83F was originally identified from a medaka (*Oryzias latipes*) cDNA library as one of a pool of genes that, when co-expressed with p53 in H1299 cells, leads to an increase in p53 abundance [27]. Salama *et al*. [26] used similar cell culture-based methods to show that FAM83F binds to and stabilizes p53 and that the interaction between FAM83F and p53 reduced the ubiquitination of the latter. Several other putative FAM83F interactors have also been identified through mass spectrometry and have yet to be explored, including Met, Ephrin B1 and 8 of the 15 human syntaxins (Gopal Sapkota, unpublished).

FAM83F is part of the 'ignorome' a term coined for the majority of protein coding genes that remain poorly characterized and to which there is little or no reference in the literature [28]. It is easier to study a gene that has already been studied [29], but to increase our understanding of biomedical science, we need to explore the roles of such proteins, particularly those implicated in human disease. These proteins are often hard to study; in the case of FAM83F, most of the experiments described in the literature are conducted in cell culture and/or by overexpression, probably because FAM83F is expressed at very low levels, and is often only detectable by immunoprecipitation [25,26]. Insights into gene function can often be gained by studying the roles they play in development, so to elucidate the role of endogenous FAM83F *in vivo*, we characterized its expression in zebrafish embryos, and used CRISPR (clustered regularly interspaced short palindromic repeats)/CRISPR-associated protein 9 (Cas-9) genome editing to KO the primary FAM83F orthologue in zebrafish, *fam83fa*. We show that loss of *fam83fa* leads to hatching defects and impairment of cellular degradation pathways, and that *fam83fa*$^{-/-}$ embryos show increased sensitivity to genotoxic stress. We show that Fam83fa protein is itself targeted to the lysosome, making it difficult to detect at the endogenous level. We propose that Fam83fa modulates autophagic processes, including larval hatching, and that impairment of autophagy following the DNA damage response causes the increased sensitivity to genotoxic stress in *fam83fa*$^{-/-}$ embryos. To our knowledge, this is the first work investigating the role of endogenous FAM83F in the physiologically relevant *in vivo* context.

2. Material and methods

2.1. Animal housing, husbandry and microinjection

All animal work, including housing and husbandry, was undertaken in accordance with The Crick Use of Animals in Research Policy, the Animals (Scientific Procedures) Act 1986 implemented by the Home Office in the UK and the Animal Welfare Act 2006. Consideration was given to the '3Rs' in experimental design. The zebrafish Zirc AB line was used as WT and as the genetic background for mutant line generation. Animals were maintained on a standard light/dark cycle, and for most zebrafish experiments, embryos were obtained by tank mass-spawning, with males and females separated overnight and barriers removed in the morning. *Xenopus laevis* embryos were obtained by *in vitro* fertilization and staged according to as previously described [30]. Embryos were maintained in Normal Amphibian Medium [31] until the four-cell stage, at which point they were injected with 500 pg of the indicated capped mRNA into a single ventral blastomere. Embryos were allowed to develop until approximately stage 35 at which point they were fixed in 4% paraformaldehyde. Embryos were then counted and scored for secondary axial phenotype classes as previously described [25].

2.2. Generation of *fam83fa*$^{-/-}$ mutant zebrafish lines

sgRNAs (single guide RNAs) were designed using CHOPCHOP [32] using the GRCz10 assembly and default search parameters. sgRNAs were selected based on their efficiency and lack of off-target effects (electronic supplementary material, table S1). The sgRNA and Cas9 protein were assembled into a ribonucleoprotein complex *in vitro* just prior to injection at the one-cell

stage, as previously described [33–36]. At 24 h post fertilization (hpf), 10 embryos from each set of injections (sgRNA1 + 3 and sgRNA2 + 4) were screened to determine mutagenesis efficiency using standard PCR and primers designed to amplify the targeted region (electronic supplementary material, table S1). Amplicons were then TA cloned (see below) and Sanger sequenced to confirm presence of indels and to determine mutagenesis efficiency (100%). The F_0 generation was then outcrossed to Zirc AB WT fish and a small number of embryos from the resulting clutch (F_1) was screened for germline transmission by PCR and TA cloning as above. As germline transmission was identified in these samples, the remaining F_1 embryos were reared to adulthood, fin-clipped and screened by PCR using the Inference of CRISPR Edits (ICE) algorithm, which allows batch analysis of CRISPR induced indels using Sanger-sequencing-generated .ab1 files [37] (see github.com/synthego-open/ice). F_1 heterozygote siblings carrying identical mutations were then incrossed to generate F_2 homozygotes, then incrossed again to generate the F_3 maternal-zygotic (MZ-) generation, as well as being maintained as heterozygous outcrossed lines. Once the precise mutations were defined, genotyping was subsequently outsourced to Transnetyx.

2.3. Cloning, plasmids and *in vitro* transcription

Total RNA was obtained from ~50 zebrafish embryos using the NucleoSpin RNA extraction kit (Macherey-Nagel). cDNA libraries were then synthesized using the SMARTer PCR cDNA Synthesis Kit (Clontech; PT4097−1) according to the manufacturer's instructions. ORFs for *fam83fa* and *fam83fb* were amplified from cDNA libraries and either TA cloned using the pGEM-T Easy Vector System (Promega) or the pENTR/D-TOPO vector system (Thermo Fisher). The *fam83fa*$^{1\text{-}500}$ construct was made using a reverse primer with a STOP codon at amino acid position 501 (electronic supplementary material, table S1). For microinjection, inserts were then subcloned into pCS2+N′ HA tagged vectors that had been converted into Gateway (Invitrogen) destination vectors, according to the manufacturer's instructions. PCR templates for *in vitro* transcription were generated from the pCS2+N′ HA–tagged destination vectors. Templates were then used in an SP6 Message Machine (Invitrogen) transcription reaction to generate capped mRNAs. The *hgg1* probe plasmid was a gift from Shingo Maegawa [38]. The pDEST-CMV-N-Tandem-mCherry-EGFP plasmid was a gift from Robin Ketteler (Addgene plasmid no. 123216; RRID: Addgene_123216) [39]. All constructs were Sanger-sequenced by the Genomics Equipment Park Science Technology Platform at the Crick.

2.4. Whole mount *in situ* hybridization (WMISH)

Digoxigenin (DIG) labelled probes were generated by *in vitro* transcription using a purified PCR template with the T7 promoter sequence at the 3′ end. (See electronic supplementary material, table S1 for primer sequences). A 20 µl reaction (DIG RNA labelling mix (Roche), T7 RNA Polymerase (Roche), 10X Transcription Buffer (Roche), Ribo-Lock RNase inhibitor (Thermo Fisher)) was used to generate the probe, which was then purified using the RNA Clean and Concentrator−5 kit (Zymo). Purified probes were quantified by nanodrop, checked for integrity by running on a 1% agarose gel and stored in hybridization buffer (50% formamide, 5X SSC, 0.1% Tween 20, 50 µg ml^{-1} heparin, 500 µg ml^{-1} Torula RNA, citric acid to pH 6) at −20°C until required. WMISH was performed as previously described [40], on embryos stored in methanol at −20°C for no longer than 1 month.

2.5. Image acquisition and live-imaging

Fixed zebrafish embryos were mounted in 2% methylcellulose on agarose coated dishes, and brightfield images captured with a Leica M165 FC microscope and a Leica DFC310 FX camera, operated by LAS v. 4.9 software. Live zebrafish imaging was performed using the same microscope. Embryos were imaged in glass bottom dishes in E2 medium. For confocal imaging, HEK293T cells were grown in µ-Slide 8-well chamber slides (Ibidi). Before imaging cells were washed in PBS. Images were obtained using a Plan-Apochromat 63×/1.40 Oil DIC M27 objective of a Zeiss inverted Axio Observer LSM 710 confocal microscope, using the 405, 543 and 639 nm laser lines to capture Z stack images. Image acquisitions and maximum intensity projections (MIPs) were performed by ZEN 2010 software. Images were processed for brightness and contrast in Fiji [41], following the principles outlined by Rossner & Yamada [42]. For the live hatching experiment, embryos were imaged in 96-well plates, with embryos arranged into three stripes: WT embryos in columns 1–4, MZ-*fam83fa*$^{-/-}$ KO1 embryos in columns 5–8 and *MZ-fam83fa*$^{-/-}$ KO2 embryos in columns 9–12. Over the course of three independent experiments, these positions were changed to mitigate for any fluctuations in temperature at any given position. U-bottomed 96-well plates were imaged on a Ti2 inverted microscope (Nikon) with motorized XY stage (ASI) and sample temperature was maintained at 28.5°C using an environmental chamber (Okolab). Brightfield images were captured of each well every hour from 32 to 80 hpf, using a 2X/0.1 NA Plan Apo objective with 1.5× intermediate magnification, with a CMOS camera (UI−3280SE, iDS) for an image pixel size of 1.15 µm. The microscope was controlled with Micro-Manager v. 2.0 software [43]. For the temporal development experiment, the imaging set up was that used in the hatching experiment and as previously described [44], with the exception of sample temperature changes where indicated.

2.6. Ionizing radiation and methyl methanesulphonate treatment

For ionizing radiation (IR) treatment, embryos were plated at a density of 50 per 100 mm dish in E2 medium. Embryos were treated in a GSR D1 caesium-137 (^{137}Cs) irradiator, on the shelf furthest away from the source to ensure even exposure. No more

than six plates were treated at any one time and irradiation times were calculated using the following equation: dose required in Gy/(dose rate in Gy min^{-1} at level 3 [0.548 Gy min^{-1} at 2019–2020]). Untreated embryos were taken to the irradiator alongside treated embryos but were not exposed. Following treatment, embryos were allowed to develop at 28.5°C. Embryo medium was changed at least once a day, with dead embryos and debris being removed daily. For methyl methanesulphonate (MMS) treatment, embryos were incubated in 250 µM MMS in 6-well plates, with 25 embryos per well, from shield stage (6 hpf) for 19 h, at which point the MMS was washed-off and replaced with E2 embryo medium. Embryos were then incubated at 28.5°C and monitored until they reached 5 days post fertilization, at which point any remaining live embryos were euthanized. A minimum of 50 embryos of each genotype were used per biological replicate ($n = 3$).

2.7. RNA-seq

Embryos treated with IR and control embryos were collected in 2 ml tubes ($n = 15$ per replicate), washed, resuspended in 350 µl RLT buffer (Qiagen) and homogenized using a 1 ml syringe with a 21G×1½′ needle. Samples were snap-frozen and stored at −80°C until all three biological replicates had been collected. Samples were then subject to automated RNA extraction using the RNeasy Mini Kit (Qiagen), with in-column DNase treatment step. RNA samples were then quantified and 25 µl of 150 ng $µl^{-1}$ of each sample was subject to Qubit quantification and Agilent TapeStation 4200 analysis to determine quality and fragment size. After QC, ribosomal RNA (rRNA) was depleted using the Ribo-Zero Plus rRNA Depletion Kit (Ilumina), followed by library preparation using the KAPA mRNA HyperPrep Kit for Illumina Platforms, both according to the manufacturer's instructions. Single read sequencing (75 bp) was then performed on the Illumina HiSeq 4000 platform. After filtering and trimming, Bowtie2 was used to map the sequencing reads to the GRCz11 assembly. There were a minimum of 15 million reads per condition, of which ≥6.5 million were uniquely mapped, and of these, ≥75% corresponded to exonic coding sequences. All data have been deposited in NCBI's Gene Expression Omnibus [45,46] and are accessible through GEO Series accession number GSE244291 (https://www.ncbi.nlm.nih.gov/geo/query/acc.cgi?acc=GSE244291). Bioinformatic analysis was performed in R (full code is available at 10.5281/zenodo.10423383) [47].

2.8. Quantitative real-time PCR (qRT-PCR)

qRT-PCR primers were designed using Primer3 (http://primer3.ut.ee/) [48], to yield an amplicon of between 75 and 200 bp, with a T_m of 60°C (± 2°C). Amplicons were designed to be intron-spanning, with a G or C at the 3′ end, a GC content of 40–60% to increase stability and low self-complementarity to avoid primer dimers. All qRT-PCR primers, whether designed externally or by using Primer3, were validated before use by standard PCR followed by efficiency testing by standard curve. Only primers with an efficiency of ≥90% (1.8–2.2), and a single melt curve, were taken forward for use in qRT-PCR experiments. Total RNA was extracted from pools of 20–25 embryos (unless otherwise stated) using either TRIzol chloroform extraction followed by isopropanol precipitation and LiCl precipitation or using the RNeasy Mini Kit (Qiagen). 1 µg of RNA was then used to synthesize cDNA in a 20 µl reverse transcription reaction using 5X First Strand Buffer and MMLV-RT (Promega) with random hexamers. 10 µl qRT-PCR reactions were performed using Precision PLUS qPCR Master Mix with SYBR green (PrimerDesign) in 384-well white plates on a Roche LightCycler 480. All qRT-PCR reactions were subject to a post PCR melt-curve to validate primer specificity, and every sample, including minus-RT and no-template controls, was run in technical triplicate. The reference gene *18S* was also run on every plate in technical triplicate. Relative gene expression values were calculated using the Livak method (ΔΔCt) [49]. Minimum Information for Publication of Quantitative Real-Time PCR Experiments guidelines [50] were followed to ensure data integrity, and all primer sequences can be found in electronic supplementary material, table S1.

2.9. Western blotting

Zebrafish embryos were manually dechorionated and transferred to non-stick tubes in batches of 25. Liquid was aspirated off and 200 µl ice-cold 50% Ginzburg Fish Ringers solution without calcium (55 mM NaCl, 1.8 mM KCl, 1.25 mM $NaHCO_3$) was added. Embryos were pipetted up and down until the yolks came away, then a further 800 µl of Ginzburg Fish Ringers solution was added. Tubes were inverted to mix, then centrifuged at 1000*g* for 3 min at 4°C. Supernatant was removed (leaving ~20 µl) and 1 ml of ice-cold wash buffer (110 mM NaCl, 3.5 mM KCl, 2.7 mM $CaCl_2$, 10 mM Tris- HCl pH 8.5) added. Tubes were shaken at 350*g* at 4°C for 5 min, then centrifuged at 1000*g* for 3 min. Cell pellets were then lysed in 100 µl per 25 embryos of freshly made lysis buffer (100 µl 1M Tris pH 8.0, 20 µl 0.5M EDTA pH 8.0, 250 µl 10% IGEPAL (NP40), 100 µl 1.25 M sodium β-glycerophosphate, 500 µl 1M NaF, 5 µl 20 µM Calyculin A, 250 µl 200 mM sodium pyrophosphate, 500 µl 10X protease inhibitor cocktail (Pierce, A32965), 3.275 ml ddH_2O) and 4X SDS (sodium dodecyl-sulphate) loading dye was added. Extracts were heated to 95°C for 10 min, allowed to cool at RT for 2–3 min, then loaded onto nUView Precast (4–20% gradient Tris-Glycine) gels (Generon) and separated by SDS-PAGE (polyacrylamide gel electrophoresis) in 1X Tris-glycine running buffer (3% Tris, 14.4% glycine, 1% SDS in H_2O). Proteins were transferred onto low fluorescence polyvinylidene fluoride (LV-PVDF) membranes in transfer buffer (3% Tris, 14.4% glycine, 0.5% SDS, 20% (*v*/*v*) methanol) using the standard 'transfer sandwich' method. Following transfer, membranes were blocked in 1X Odyssey Blocking Buffer (TBS) (LI-COR) in TBS. Membranes were incubated overnight in primary antibodies in blocking buffer (anti-p53, ab77813 [9.1] [51]), 1:200, anti-β-actin, (CST C4967),

1:1000, anti-HA, (Sigma H3663), 1:1000) before washing in TBST (TBS+0.1% Tween) and overnight incubation in secondary antibodies (Goat anti-rabbit IRDye 680 RD and anti-mouse IRDye 800 CW (LI-COR), 1:10 000) in TBST with 0.02% SDS at RT. Membranes were washed, then imaged on the LI-COR Odyssey imaging system in the 700 and 800 nm channels. Images were processed for brightness and contrast in Adobe Photoshop CC (2019) following the principles outlined by Rossner & Yamada [42]. Western blotting densitometry quantification was performed by importing the .tiff file into Fiji [41], thresholding, analysing particles and measuring mean grey values. Values for experimental bands were then normalized to the input bands and either plotted accordingly or expressed as a fold change value where indicated. The p53 antibody was additionally validated by western blotting protein extracts from zebrafish embryos exposed to a dose-response of IR (20, 30 and 40 Gy), to confirm increasing abundance of p53 protein (data not shown).

For *Xenopus*, embryos were obtained as described above and injected into the animal hemisphere at the one-cell stage with 500 pg of the indicated capped mRNA. Embryos were allowed to develop to stage 10 before being lysed in 10 µl per embryo ice-cold lysis buffer (1% IGEPAL, 150 mM NaCl, 10 mM HEPES, pH 7.4, 2 mM EDTA and protease inhibitor cocktail [A32965; Pierce]). Lipids and yolk were removed from the lysate by Freon extraction (equal volume), and the aqueous phase was collected following centrifugation for 15 min at 4°C. Protein extracts were then denatured in SDS buffer before being separated by SDS–PAGE as described.

2.10. Cell culture and tandem fluorescence assay

HEK293T cells were cultured in DMEM, high glucose (Gibco, Thermo Fisher Scientific) containing 10% Foetal Bovine Serum (Thermo Fisher Scientific). Cells were passaged at 80% confluency using TrypLE Express (Thermo Fisher Scientific). For transfections cells were grown in µ-slide 8-cell chamber slides (Ibidi). Cells were transfected with a plasmid containing tandem fluorescent proteins GFP/mCherry (empty vector, EV), tandem GFP/mCherry fluorescently tagged Fam83fa protein and tandem GFP/mCherry fluorescently tagged truncated Fam83fa$^{1\text{-}500}$ protein (37.5 ng per well) using FuGENE HD transfection reagent as per the manufacturer's guidelines. After 24 h of transfection, cells were treated with 50 µM Bafilomycin for 2 h.

3. Results

3.1. Fam83fa is expressed in the embryonic hatching gland

The zebrafish genome was interrogated to obtain the coding sequence for the open reading frame (ORF) of *fam83f*. Due to genome duplication, zebrafish frequently have more than one orthologue of a human gene (reviewed in [52]) and *fam83f* is no exception with two orthologues, *fam83fa* and *fam83fb*, both containing five exons, on chromosomes 3 and 6, respectively. Fam83fa most closely aligns to FAM83F in human and other species (including mouse and *Xenopus*; electronic supplementary material, figure S1A) and contains the F-x-x-x-F sequence motif required for CK1α interaction [23,25]. Furthermore, human (and mouse and *Xenopus*) FAM83F has a C′ terminal CaaX box consisting of an invariant cysteine, two aliphatic amino acids and a terminal amino acid 'X'. This CaaX box motif is recognized by prenylation enzymes which add either a farnesyl or geranylgeranyl moiety to the cysteine residue, targeting the protein to cell membranes [53]. Zebrafish Fam83fa, despite not having a 'canonical' CaaX box at the C′ terminus, is still predicted to be farnesylated in the same way as human FAM83F, on the invariant cysteine residue of the C′ terminal CIQS sequence [54] (electronic supplementary material, figure S1B). By contrast, Fam83fb is 108 aa shorter than Fam83fa (447 aa compared with 555 aa) and does not contain any C′ terminal residues that are predicted to be prenylated. Moreover, whereas overexpression of Fam83fa causes a secondary axis in *Xenopus* embryos [25], overexpression of Fam83fb does not (electronic supplementary material, figure S1C). It is therefore likely that Fam83fa is the orthologue most closely resembling human FAM83F and we termed this the primary orthologue.

According to the White *et al*. [55] RNA-seq dataset and our qRT-PCR data (figure 1*a*), *fam83fa* is expressed maternally, between 2 and 4 hpf, with expression levels dropping off after zygotic genome activation (ZGA, ~4 hpf) and peaking again around 24–48 hpf, albeit at a lower level. Whole mount *in situ* hybridization confirmed that *fam83fa* is expressed at late gastrula stage (90% epiboly) in the pre-polster, a distinct group of mesendodermal cells located underneath the developing forebrain from around 75% epiboly (8 hpf) [56] (figure 1*b*). As this group of cells arises from the anterior axial hypoblast at around 8 hpf [57], this expression profile was in keeping with the qRT-PCR data, which showed that following ZGA, levels of *fam83fa* transcript start to increase after 8 hpf. The pre-polster becomes the polster by the end of gastrulation and by 12 hpf, it was visible as a U-shaped mesendodermal structure in front of the boundary of the anterior neural plate (figure 1*c*). The polster itself is part of the pre-chordal plate and is the rudiment to the hatching gland [58–60]. As development progresses, the polster cells migrate in an anterodorsal direction to fan out across the yolk sac where they form the hatching gland proper [56,61], and by 18 hpf *fam83fa* expression was restricted to the early hatching gland (figure 1*d*). *fam83fa* expression in the hatching gland was apparent at 24 hpf and continued to persist at 48 hpf (figure 1*e–f*).

The hatching gland is a specialized temporary structure present in the embryos of anuran amphibians and fish species, including teleost embryos such as zebrafish [62]. The primary role of the hatching gland is to release proteolytic enzymes that soften the surrounding chorion [63]. This chorion softening, combined with the spontaneous movement of the larvae, allows hatching to occur, usually sometime between 48 and 72 hpf [64]. To validate the spatial domain of *fam83fa* expression, we performed whole mount *in situ* hybridization for *hatching gland gene 1* (*hgg1*), also known as *cathepsin Lb* (*ctslb*), an endopeptidase expressed in hatching gland cells at 24 hpf [63,65,66]. The spatial expression domain of *hgg1* matched that of *fam83fa*, confirming that *fam83fa* is expressed in the hatching gland of the zebrafish embryo (figure 1*g–i*).

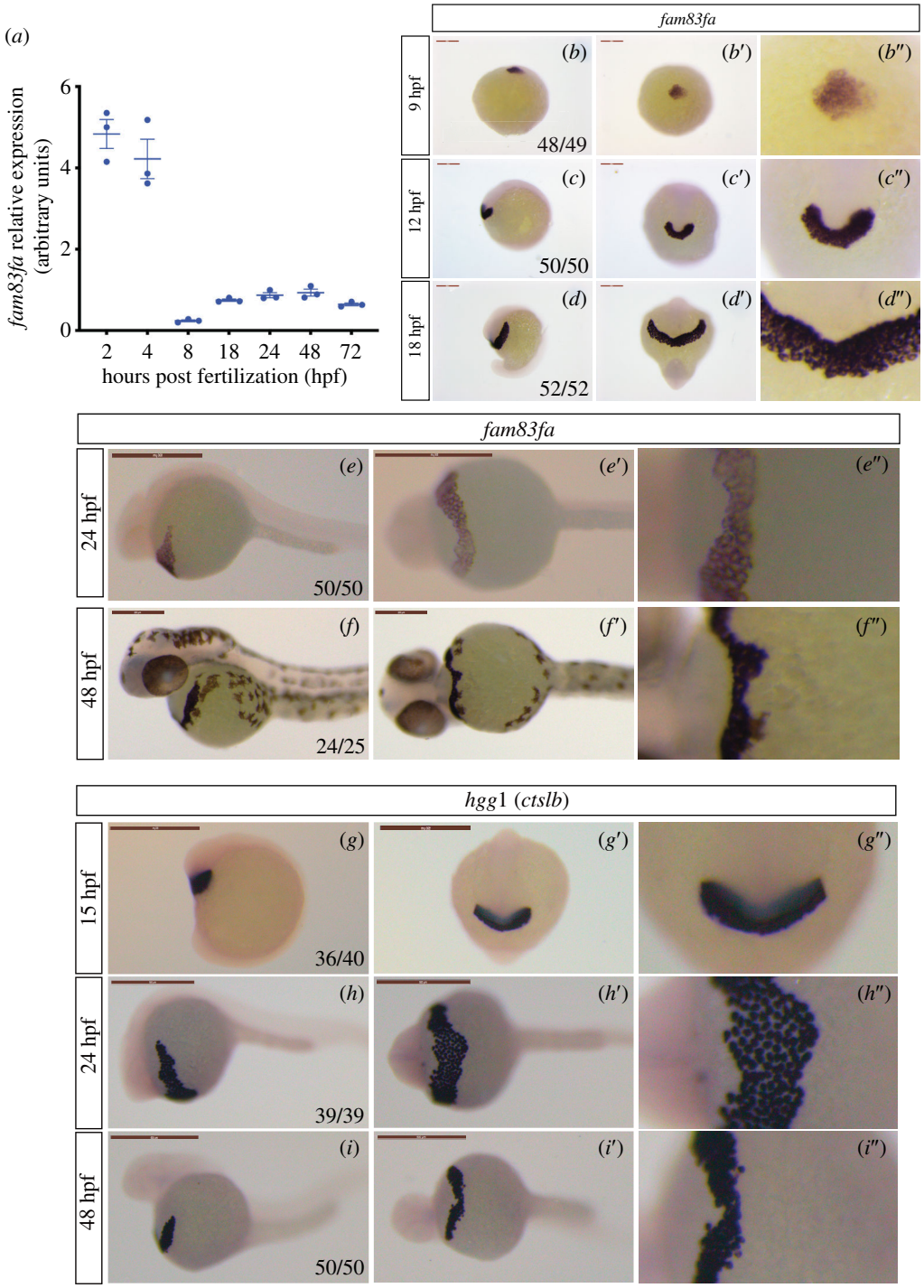

Figure 1. Zebrafish *fam83fa* is expressed in the hatching gland (*a*) qRT-PCR of *fam83fa* expression (arbitrary units) in whole embryos across developmental time-series as shown. Data points = one biological replicate, $n = 3$. Error bars = s.e.m. All data normalized to *18S* and calculated using the ΔΔCt (Livak) method. (*b–f*) *fam83fa* expression by whole mount *in situ* hybridization in stages as labelled. Lateral views (*b–f*), dorsal (*b*) or ventral views (*c′–f′*) and zoomed in regions of centre image (*b″–f″*) shown. Numbers of embryos are denoted in first image. *fam83fa* is expressed in the pre-polster, the polster and the hatching gland. Scale bars = 250 µm (except 24 hpf = 500 µm). (*g–i*) *hgg1* expression by whole mount *in situ* hybridization in stages as labelled. Lateral views (*g–i*), anterior (*g′*) or ventral views (*h′–i′*) and zoomed in regions of centre image (*g″–f″*) shown. Scale bars = 500 µm.

3.2. Generation of *fam83fa*$^{-/-}$ zebrafish lines

Most *in vivo* studies into the role of FAM83F have used overexpression assays, but the best way to infer the biological function of a gene is to assess the effect of its KO. We therefore used CRISPR/Cas9-mediated KO approaches to generate stable *fam83fa*$^{-/-}$ zebrafish lines.

One consideration in our KO strategy was the issue of functional redundancy, where a gene (usually a member of the same family) assumes the function of the absent gene, resulting in no apparent (or a mild) phenotype [67]. We also took into account the phenomenon of genetic compensation, where another gene is upregulated to compensate for the deleted gene's function, a phenomenon that occurs in genetic mutants but not in morphants [68]. This transcriptional adaptation occurs in response to mutant mRNA decay and compensatory genes are transcriptionally upregulated in a sequence specific manner [69]. With these

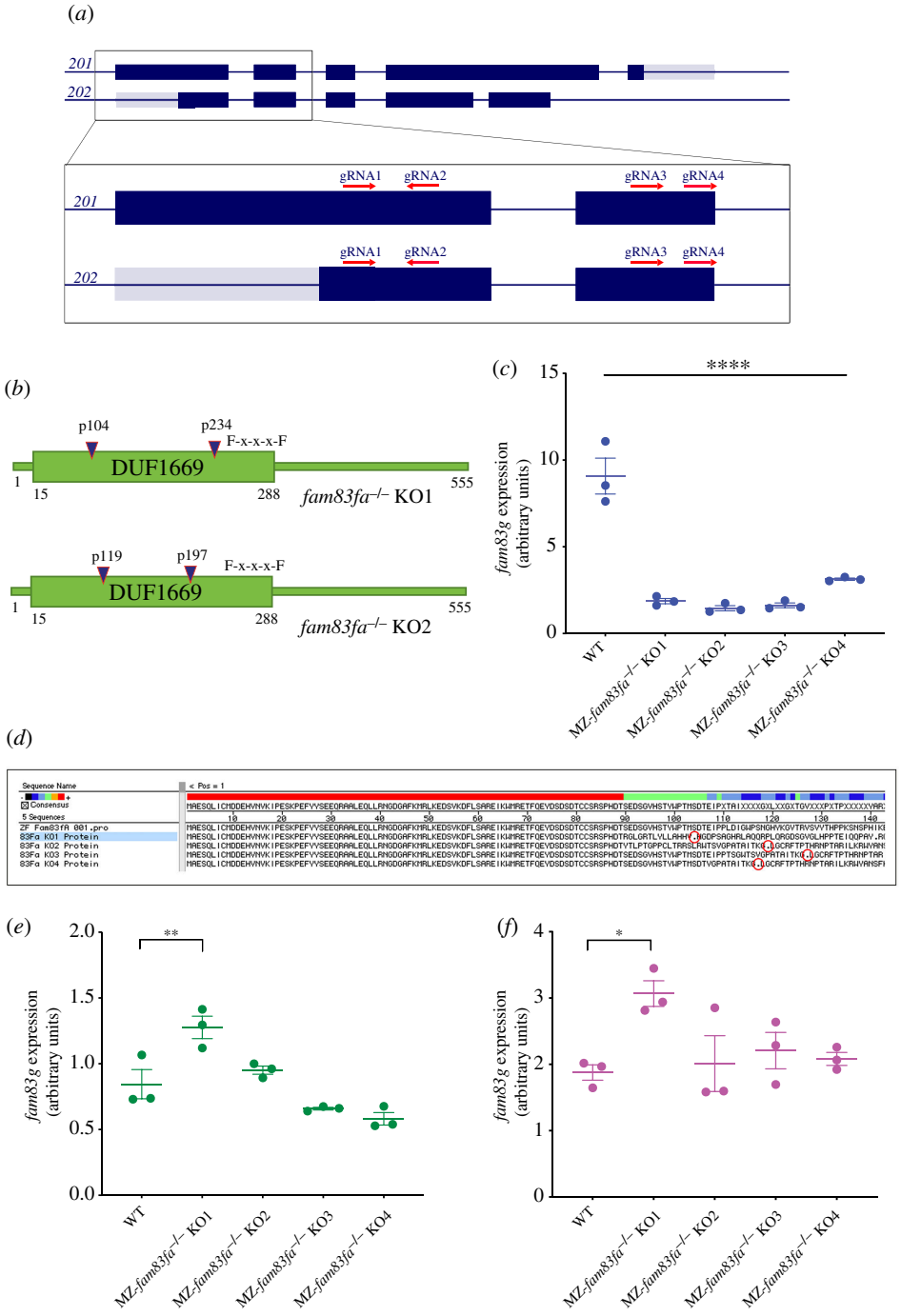

Figure 2. Generation of *fam83fa*$^{-/-}$ zebrafish lines by CRISPR/Cas9 (*a*) Schematic representation of *fam83fa* transcripts *201* and *202* showing CRISPR/Cas9 gRNA targeting regions. Dark blue and grey boxes denote exons and untranslated exonic regions, respectively. Zoomed region shows exons 1 and 2 and the gRNA (1–4) target regions (red arrows). Transcript *201* is the presumed primary transcript; however, all gRNAs were designed to promote complete loss of the DUF1669 domain by introducing indels at the 5′ end of either transcript. (*b*) Schematic of Fam83fa showing locations of the PTCs induced in the *fam83fa*$^{-/-}$ KO1 and KO2 lines by combined injection of gRNA1+ gRNA3 (blue triangles). Exons 1 and 2 (*a*) code for the first 210 aa of Fam83fa, therefore all gRNAs were predicted to induce PTCs in the DUF1669 domain upstream of the F-x-x-x-F sequence motif (for simplicity, only KO1-KO2 are shown). (*c*) Relative expression of *fam83fa* in WT and MZ-*fam83fa*$^{-/-}$ KO1–KO4 homozygous embryos as labelled, normalized to *18S* (arbitrary units). Data points represent biological replicates. Error bars = s.e.m. ****$p < 0.00005$, one-way ANOVA with Tukey's post-hoc test. (*d*) *In silico* translation of the Sanger sequenced qRT-PCR products amplified in (*c*). PTCs are denoted by red circles. Alignment performed using MegAlign software (DNASTAR). (*e*) Relative expression of *fam83fb* in WT and MZ-*fam83fa*$^{-/-}$ KO1–KO4 homozygous embryos as labelled, normalized to *18S*. Error bars = s.e.m. **$p < 0.005$; *$p < 0.05$, one-way ANOVA with Tukey's post-hoc test. Data points represent biological replicates. (*f*) As (*e*) except showing relative expression of *fam83g*.

points in mind, we decided to generate four different *fam83fa*$^{-/-}$ KO lines to increase the probability that at least one line would escape these compensatory mechanisms and be more likely to show a phenotype.

Four guide RNAs (gRNAs) were designed using the online program CHOPCHOP [32] to target both transcript variants of *fam83fa* leading to complete loss of the DUF1669 domain (figure 2*a*). To increase the probability that a double-stranded break would be induced in the injected embryos, gRNA 1+3 RNP (ribonucleoprotein) complexes and gRNA 2+4 RNP complexes were injected together, to target exons 1 and 2 simultaneously. Screening of >100 animals at the F_1 generation, using a combination of MiSeq next generation sequencing and Sanger sequencing, confirmed the high efficiency of this approach (data not shown).

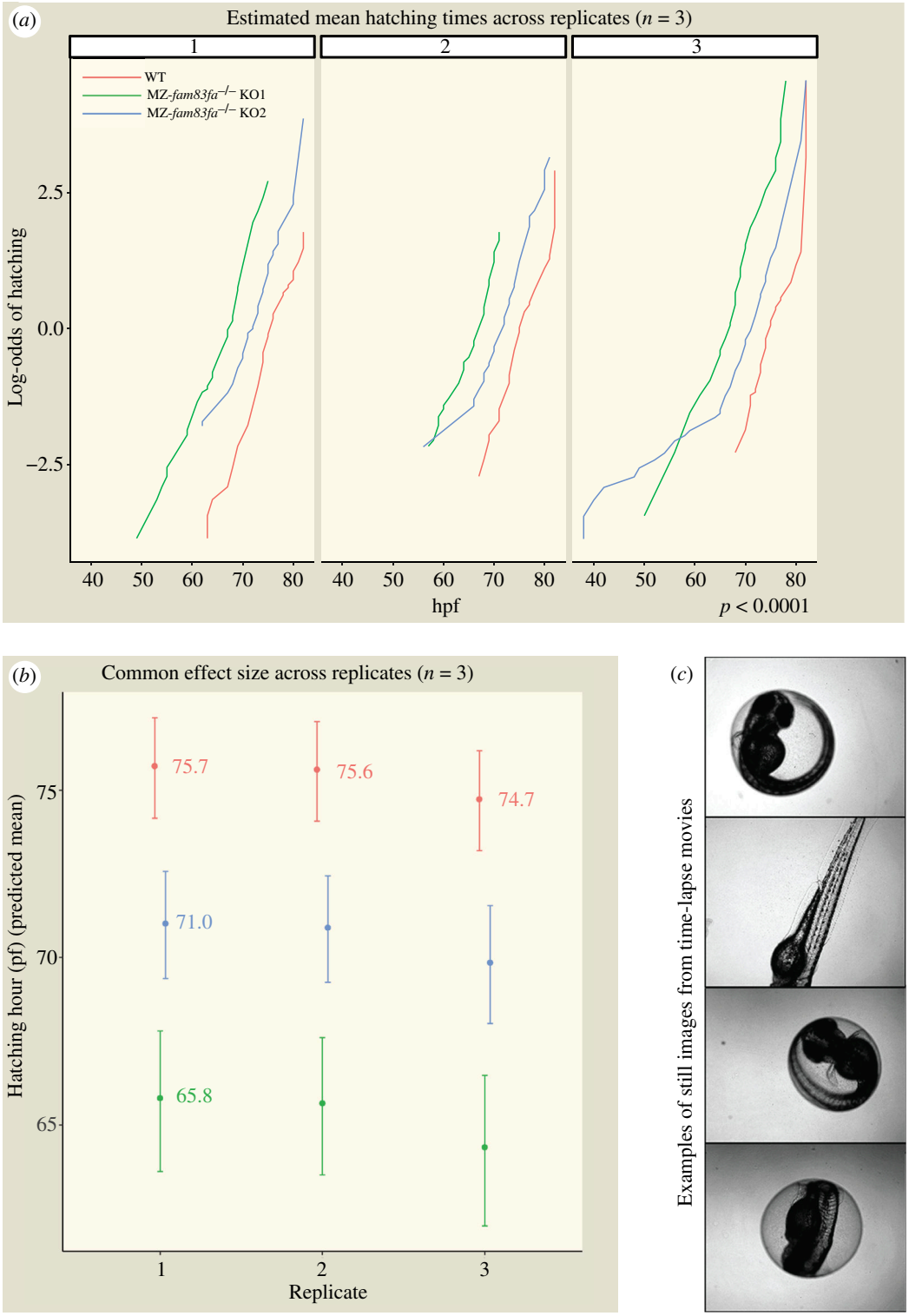

Figure 3. MZ-*fam83fa*$^{-/-}$ mutant embryos hatch earlier than WT. (*a*) Estimated mean hatching times across replicates ($n = 3$) for WT (red), MZ-*fam83fa*$^{-/-}$ KO1 (green) and MZ-*fam83fa*$^{-/-}$ KO2 (blue). Log-odds of hatching is plotted over time (hpf); where the curves cross 0.0 on the *y*-axis, 50% of the embryos have hatched. $p < 0.0001$, proportional odds logistic regression. (*b*) Common effect size across replicates shown as predicted mean hatching hour. Note that MZ-*fam83fa*$^{-/-}$ KO1 embryos hatch ~10 h earlier than WT. (*c*) Examples of still images from time-lapse movies used to determine hatching times.

Of these fish, we selected four genotypes where the induced mutations were predicted to induce a premature termination codon (PTC) upstream of the F-x-x-x-F sequence motif (F275/F279), as a result of a shift in the ORF. These four genotypes were denoted *fam83fa*$^{-/-}$ KO1-KO4 (electronic supplementary material, table S2), and schematic representations of KO1 and KO2 are shown in figure 2*b*. As no commercial Fam83fa antibody is available, we validated our *fam83fa*$^{-/-}$ KO lines at the mRNA level. mRNAs harbouring a PTC that is 50–55 nucleotides upstream of the last exon:exon boundary trigger the non-sense-mediated decay (NMD) pathway and are degraded [70]. We predicted that all four of our *fam83fa*$^{-/-}$ KO lines would show reduced levels of *fam83fa* transcripts, which we confirmed by qRT-PCR (figure 2*c*). All four F_3 generation maternal-zygotic (MZ-) *fam83fa*$^{-/-}$ KO lines showed reduced levels of *fam83fa* mRNA to a similar extent, with KO1 and KO2 being most severely affected; transcripts were undetectable using a second primer set (electronic supplementary material, figure S2A). Sanger sequencing of the qRT-PCR amplicons confirmed that all predicted PTC mutations induced in the genome had been carried forward in

the residual mRNA/cDNA (figure 2*d*), confirming that all four MZ-*fam83fa*$^{-/-}$ KO lines were functionally null. Interestingly, qRT-PCR showed that in MZ-*fam83fa*$^{-/-}$ KO1, levels of both *fam83fb* and *fam83g* were significantly upregulated compared to both WT and the other three MZ-*fam83fa*$^{-/-}$ KO lines. This suggests that the specific mutation induced in KO1 is triggering a transcriptional adaptation response [69] that is absent in the other MZ-*fam83fa*$^{-/-}$ KO lines (figure 2*e–f*).

Having validated our *fam83fa*$^{-/-}$ KO lines, we sought to identify any phenotype associated with loss of *fam83fa*. For practical reasons, we proceeded with all subsequent experiments using two of the four MZ-*fam83fa*$^{-/-}$ lines: MZ-*fam83fa*$^{-/-}$ KO1 and KO2. These lines were selected because of the putative presence and absence of a transcriptional adaptation response, respectively.

3.3. MZ-*fam83fa*$^{-/-}$ phenotype characterization

fam83fa is expressed in the hatching gland (figure 1), so we asked whether hatching is affected in MZ-*fam83fa*$^{-/-}$ embryos. WT and MZ-*fam83fa*$^{-/-}$ KO1 and KO2 embryos were incubated at 28.5°C until they reached 24 hpf, at which point 32 embryos from each line were transferred into individual wells of a 96-well plate. Each well was maintained at 28.5°C and imaged every hour from 32 to 80 hpf. Time-lapse movies of the images captured were then manually analysed to determine the time at which each embryo hatched (figure 3*c*). Both MZ-*fam83fa*$^{-/-}$ KO lines hatched significantly earlier than WT counterparts (figure 3*a*). MZ-*fam83fa*$^{-/-}$ KO1 embryos were more severely affected, with hatching occurring on average 10 h earlier than WT embryos, compared with 5 h earlier for KO2 (figure 3*b*). This suggests that *fam83fa* is involved in the temporal regulation of larval hatching, and that loss of *fam83fa* leads to loss of this temporal control. The primary purpose of the chorion is to protect the embryo from the external environment [71] and therefore the length of time for which the embryo remains within the chorion is crucial to its survival chances [72].

We went on to ask whether premature hatching might be secondary to a general acceleration of development. We were unable manually to detect any differences in developmental rate in MZ-*fam83fa*$^{-/-}$ embryos compared with WT, but to test this in an unbiased fashion, we used a machine-learning based object classification algorithm that enables the temporal trajectory of mutant embryos to be directly compared with their WT counterparts [44]. Images were obtained of 96 embryos from WT and the most severely affected line, MZ-*fam83fa*$^{-/-}$ KO1, every 15 min from 4 to 18 hpf, then assessed by the classifier. These data confirmed there are no temporal developmental abnormalities in MZ-*fam83fa*$^{-/-}$ KO1 embryos—they develop at the same rate as WT (electronic supplementary material, figure S3). Our findings therefore demonstrate that loss of *fam83fa* in developing zebrafish embryos directly accelerates the hatching programme.

3.4. MZ-*fam83fa*$^{-/-}$ embryos show increased sensitivity to DNA damage

With the exception of premature hatching, MZ-*fam83fa*$^{-/-}$ KO1 and KO2 embryos displayed no obvious phenotype. It is not unusual for KO embryos to appear normal under laboratory conditions, because some phenotypes only manifest themselves in response to specific challenges [73–76]. With this in mind, we noted that Salama *et al*. [26] demonstrated that FAM83F stabilizes p53 and promotes its activity, so we first asked whether MZ-*fam83fa*$^{-/-}$ KO embryos, in which p53 levels may be reduced, are less susceptible to cell death induced by DNA damage, as observed in *p53*$^{-/-}$ null zebrafish [77]. To this end, we treated embryos from each genotype (WT, MZ-*fam83fa*$^{-/-}$ KO1 and MZ-*fam83fa*$^{-/-}$ KO2) with IR. Interestingly, MZ-*fam83fa*$^{-/-}$ KO1 and KO2 embryos were more severely affected by IR than were their WT counterparts in terms of morphological defects (bent body axis, oedema) and lethality, with MZ-*fam83fa*$^{-/-}$ KO1 again being the more severely affected (electronic supplementary material, figure S4A–B). Similar results were observed with the DNA damage-inducing agent MMS (electronic supplementary material, figure S4C–D).

The increased sensitivity of MZ-*fam83fa*$^{-/-}$ KO embryos to IR treatment suggests that Fam83f does not stabilize p53 in the early zebrafish embryo. To corroborate this conclusion, we extracted protein from WT and IR treated MZ-*fam83fa*$^{-/-}$ mutant embryos and analysed p53 levels by western blotting (figure 4*a,b*; electronic supplementary material, figure S5). p53 was undetectable in untreated embryos (figure 4*a*; electronic supplementary material, figure S5) and, as expected, there was significant induction in all IR-treated samples. However, there was no detectable difference in p53 levels in MZ-*fam83fa*$^{-/-}$mutants compared with WT embryos at either 2 (t1) or 10 (t2) h following IR treatment. Similarly, qRT-PCR for *p53* and its downstream targets *mdm2*, *p21*, *puma* and *bax* [77,78] showed significant upregulation in all embryos following IR treatment, but we detected no difference between WT and MZ-*fam83fa*$^{-/-}$ mutant embryos (figure 4*c–d*). These data suggest that loss of *fam83fa* does not affect the stability of p53.

3.5. RNA-seq reveals downregulation of phosphatidylinositol-3-phosphate (PI(3)P) binding proteins in MZ-*fam83fa*$^{-/-}$ embryos

If not through p53 stability, why is it that MZ-*fam83fa*$^{-/-}$ embryos are more sensitive to DNA damage? To address this question, we performed bulk RNA-seq on IR-treated and untreated embryos of each genotype. Total RNA was extracted from pools of 15 embryos 2 h after treatment, with additional pools being harvested 8 h later, because the DNA damage response involves early and later steps [79] (electronic supplementary material, figure S6A).

Principal component analysis showed that most variance is described by four components (electronic supplementary material, figure S6B). Principal component 1 (PC1) accounts for developmental time (26 hpf versus 34 hpf) and PC2 accounts

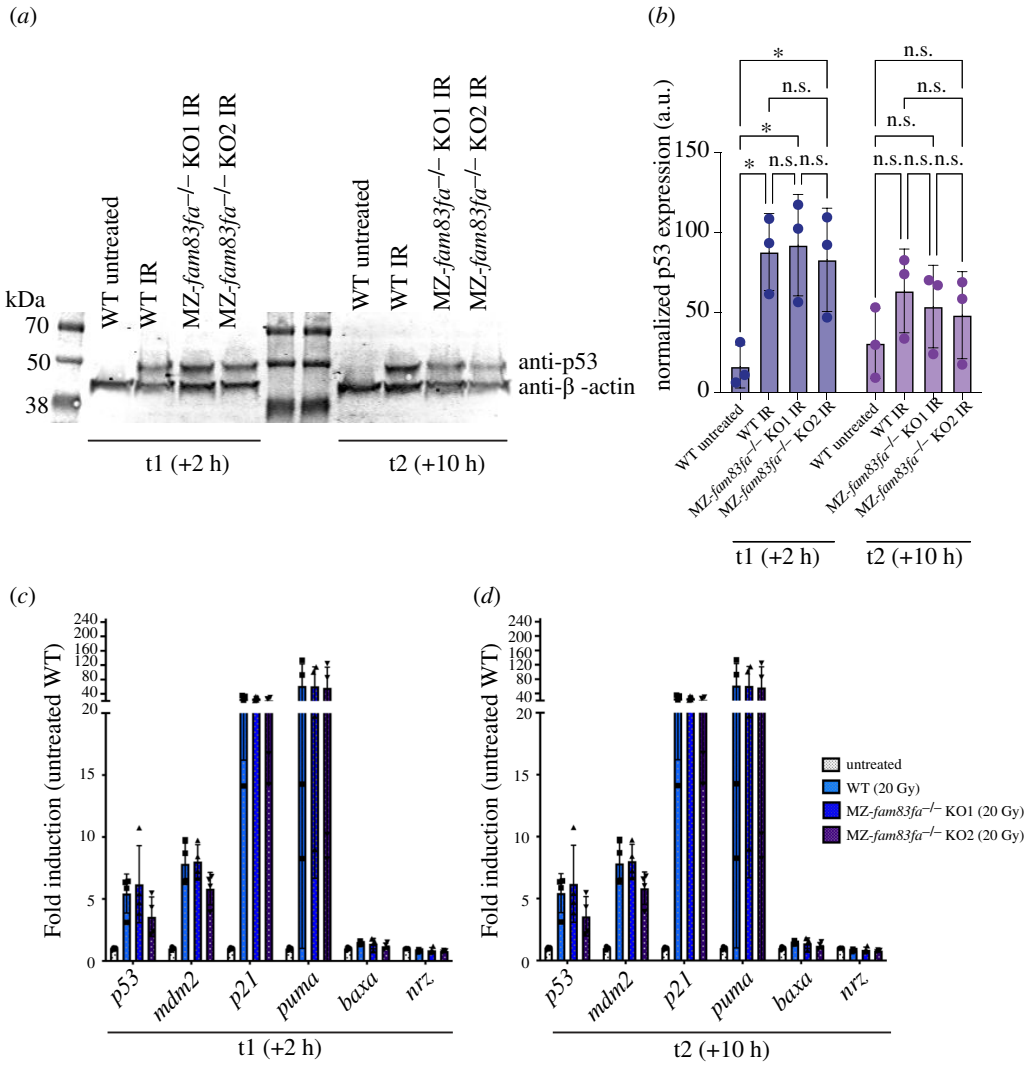

Figure 4. No difference in the p53 response was detected in MZ-*fam83fa*$^{-/-}$ embryos compared with WT. (*a*) Representative western blot for p53 and β-actin (input) in protein extracts from zebrafish embryos treated with IR at 24 hpf and harvested for protein extraction 2 h (t1) and 10 h (t2) after treatment. (*b*) Quantification of p53 band density for three independent experiments as represented in (*a*), normalized to β-actin and expressed as arbitrary units. *$p < 0.05$, two-way ANOVA with Šídák's multiple comparison test. n.s. = not significant. Error bars = s.d. (*c*) qRT-PCR of mRNA extracted from WT or MZ-*fam83fa*$^{-/-}$ KO embryos as labelled, 2 h following treatment with IR at 24 hpf. qRT-PCR was performed for p53 target genes, including *p53* itself, and *nrz*, the zebrafish *bcl–2* homologue. Data represent mean of four biological replicates (data points), each consisting of 25 embryos per line, normalized to *18S* and expressed as fold induction relative to untreated WT. (*d*) Same as (*c*) except at 10 h following IR treatment. Two-way ANOVA with Tukey's post-hoc test showed no significant differences between IR-treated WT and MZ-*fam83fa*$^{-/-}$ KO for any gene tested. Error bars = s.d.

for treatment with IR (electronic supplementary material, figure S6C). PC3 appears to represent the three genotypes (WT, MZ-*fam83fa*$^{-/-}$ KO1 and KO2), which separate roughly into three horizontal lines (electronic supplementary material, figure S6D). Most intriguingly, PC4 appears to represent the effect of loss of *fam83fa* (electronic supplementary material, figure S6E). Here, MZ-*fam83fa*$^{-/-}$ KO1 and KO2 samples cluster together on one horizontal line, clearly separate from WT. The variations underpinning PC4 may therefore be direct results of the KO of *fam83fa*, and we explored this using differential gene expression analysis.

Our analysis used DESeq2 [80]. Only genes with an adjusted *p*-value (*p* adj.) less than 0.05 and a log2 fold change (log2FC) of ±0.5 were defined as differentially expressed genes (DEGs). The use of two different MZ-*fam83fa*$^{-/-}$ lines allowed us to remove up or down-regulated differentially expressed genes that are specific to just one mutant line (figure 5*a–c*); DEGs that both lines have in common are more likely to be due directly to the loss of *fam83fa*, and to underpin the variance identified by PC4 (electronic supplementary material, figure S6E).

DEGs common to both MZ-*fam83fa*$^{-/-}$ KO1 and KO2 (Venn diagram intersections, figure 5*a–c*) were used to make a heatmap (figure 5*d*). Several genes were consistently upregulated or downregulated in both MZ-*fam83fa*$^{-/-}$ KO lines at both timepoints (scatter plots, figure 5*e–f*). Upregulated genes include intelectins 1 and 2 (*ITLN1* and *si:ch211–194p6.10*), carbohydrate binding proteins involved in phagocytosis [81,82], the lipid transport gene vitellogenin 7 (*Vtg7*) and several autophagy/lysosome-related genes including *galcb*, *arl8bb* and the autophagy associated microtubule-binding protein *map1lc3b*. Downregulated genes include *si:ch211–108d22.2*, an ATP binding protein predicted to be involved in apoptosis, and *chadla*, a transmembrane protein involved in the inflammatory response. Strikingly, the most significantly downregulated genes in MZ-*fam83fa*$^{-/-}$ KO embryos across all conditions and all time-points code for predicted PI(3)P binding proteins, including *zgc:173443* and *si:ch211–251f6.7* (figure 5*e–f*; electronic supplementary material, figure S6F). PI(3)P binding proteins are also significantly downregulated in MZ-*fam83fa*$^{-/-}$

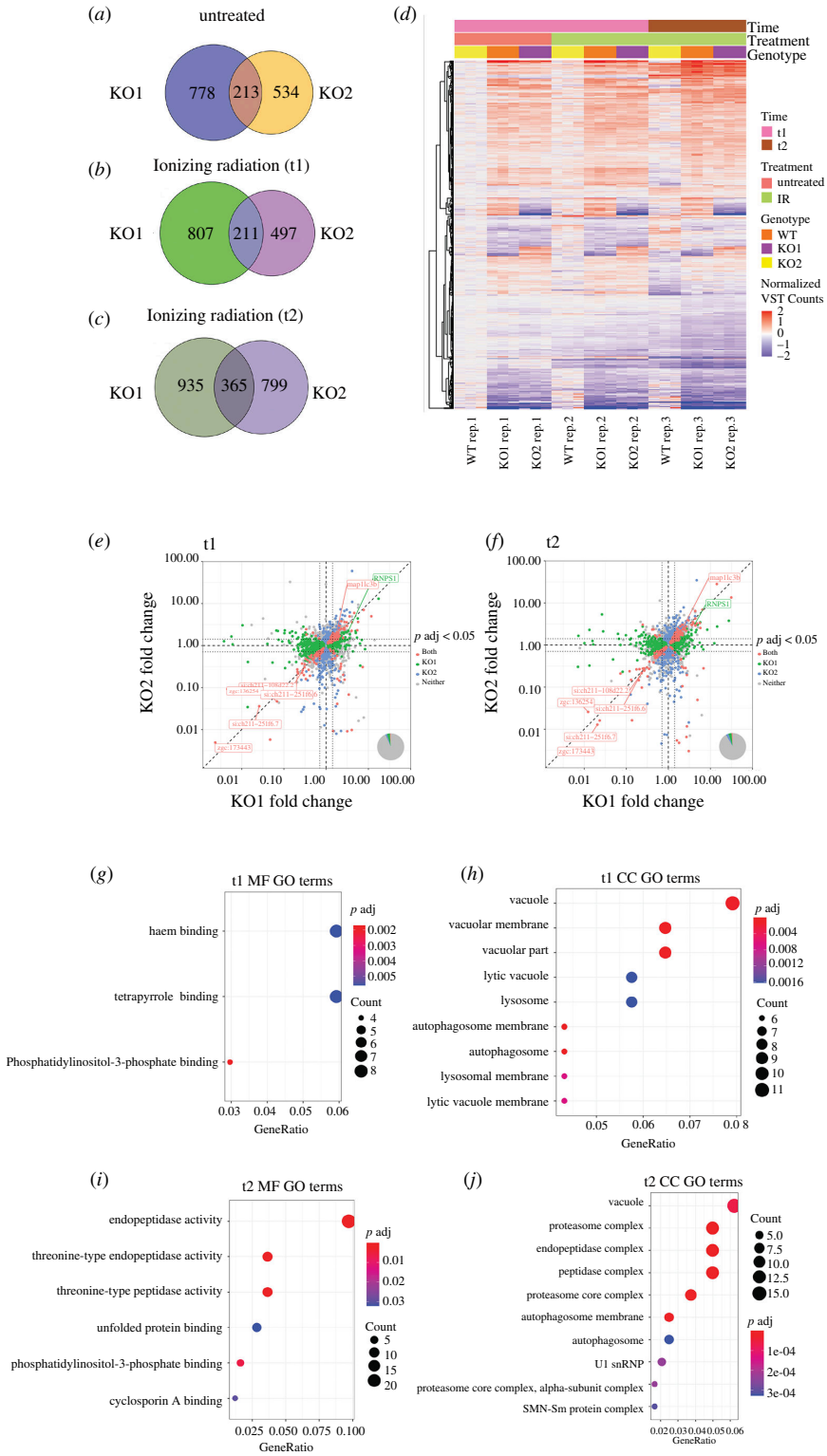

Figure 5. Transcriptomic analysis suggests degradation pathways are impaired in MZ-*fam83fa*$^{-/-}$ embryos (*a*) Venn diagram showing the DEGs in untreated MZ-*fam83fa*$^{-/-}$ KO1 and KO2 embryos compared to WT at t1 (26 hpf). (*b*) and (*c*) As (*a*) except IR treated embryos at t1 (26 hpf—2 h post IR treatment) and t2 (34 hpf—10 h post IR treatment), respectively. (*d*) Heat map of DEGs common to both KO1 and KO2 (from Venn diagram intersections above) using Euclidean distance to cluster rlog-transformed data, at conditions/times as labelled. Data displayed as normalized variance stabilized count. (*e*) Volcano plot of fold change in MZ-*fam83fa*$^{-/-}$ KO1 and KO2 (*x*- and *y*-axes, respectively) of genes with Padj < 0.05, at t1. Vertical and horizontal dashed lines represent no change in KO1 or KO2, respectively, diagonal dashed line represents identical fold change in both KO1 and KO2. Dotted lines represent log2 fold change threshold of ±0.5. Venn diagram in bottom right shows the proportion of genes in each category as shown in the legend. (*f*) Same as (*e*) except at t2. (*g*) MF GO terms for DEGs common to both MZ-*fam83fa*$^{-/-}$ KO1 and KO2 at t1 (intersection of Venn diagram in (*b*)). (*h*) Same as (*g*) except CC GO terms. (*i*) MF GO terms for DEGs common to both MZ-*fam83fa*$^{-/-}$ KO1 and KO2 at t2 (intersection of Venn diagram in (*c*)). (*j*) Same as (*i*) except CC GO terms. CC, cellular component; GO, gene ontology; MF, molecular function.

KO embryos following IR treatment, including *si:ch211–251f6.7* and *zgc:136254*. Little is known about the roles of these genes, but they are predicted to have PI(3)P binding activity and to localize to the autophagosome/lysosome membrane [83]. A study by Yilmaz et al. [84] showed that several of these predicted PI(3)P binding proteins are downregulated in *vtg3* KO zebrafish eggs, in which they also observed a concomitant upregulation of *vtg7*. This observation is in line with our dataset, suggesting a

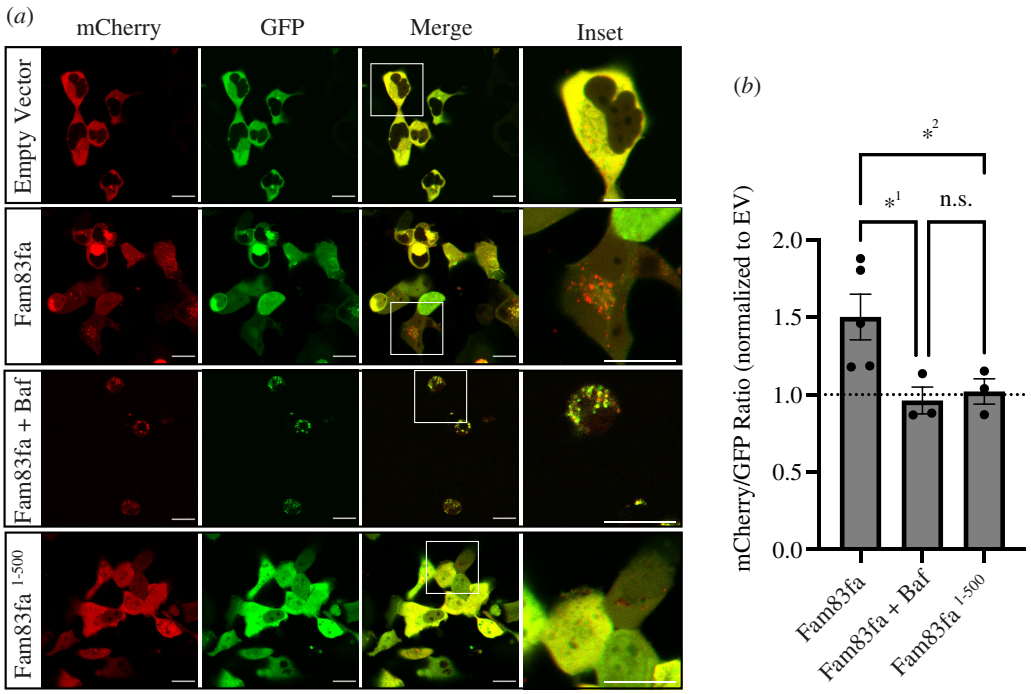

Figure 6. Fam83fa is targeted to the lysosome. (*a*) Representative confocal images showing HEK293T cells transfected with a plasmid containing tandem fluorescent proteins GFP/mCherry (empty vector, EV), tandem GFP/mCherry fluorescently tagged Fam83fa protein, with or without Bafilomycin A1 (Baf) and tandem GFP/mCherry fluorescently tagged truncated Fam83fa$^{1\text{-}500}$ protein as labelled. Scale bars = 20 µm. (*b*) Ratio of mCherry/GFP in all conditions shown in (*a*). Ratio of each biological repeat (independent transfection) is displayed normalized to empty vector control. Error bars = s.e.m. *$^1p = 0.0203$ and *$^2p = 0.0330$, Fisher's LSD test, n.s. = not significant.

functional link between these genes. Interestingly, *rnps1,* which codes for an RNA binding protein important for NMD [85], was only upregulated in MZ-*fam83fa*$^{-/-}$ KO1, suggesting it plays a role in the transcriptional adaptation response observed in this line (figures 5*e–f* and 2*e–f*).

Gene ontology (GO) analysis of our dataset demonstrated that genes associated with lysosomes, vacuoles and autophagosomes were significantly represented 2 h after IR treatment (t1), with the majority being upregulated in both MZ-*fam83fa*$^{-/-}$ KO1 and KO2 embryos compared to WT. These genes include *lamp2* (lysosomal-associated membrane protein 2), *man2b1* (mannosidase alpha 2b1) and *map1lc3b* (microtubule-associated protein 1 light chain beta 3) (figure 5*g–h*), all of which are involved in lysosomal degradation pathways [86] (reviewed in [87]). By 10 h after IR treatment (t2), GO terms showed enrichment for genes involved in endopeptidase activity and the unfolded protein response (UPR), as well as genes associated with autophagosomes, vacuoles and the proteasome (figure 5*i–j*). Upregulated endopeptidase genes at t2 include *furina, dpp4, capn2a, casp8l2*, while upregulated lysosome and vacuole associated genes at t2 include *lamp2, man2b1, vac14, galca, galcb, map1lc3b* and others. In addition to the PI(3)P binding proteins, downregulated genes at t2 included several proteasomal subunit genes, UPR genes such as *hspa9* (heat shock protein A9), and cyclosporin A binding proteins. All data have been deposited in NCBI's Gene Expression Omnibus [88] and are accessible through GEO Series accession number GSE244291 (https://www.ncbi.nlm.nih.gov/geo/query/acc.cgi?acc=GSE244291).

The increased sensitivity of MZ-*fam83fa*$^{-/-}$ KO embryos to DNA damage might be associated with the downregulation of PI(3)P binding proteins described above. Loss of these proteins would compromise autophagy [89,90], which is usually activated by genotoxic stress and is cytoprotective thanks to its role in clearing unfolded or damaged proteins [91]. Impairments in autophagic pathways have been shown to render cells more vulnerable to genotoxic agents, indeed, some anticancer therapies are based on impairment of autophagic pathways [92]. Premature hatching of MZ-*fam83fa*$^{-/-}$ KO embryos might also be explained by defects in autophagy; hatching gland cells contain large granules of proteolytic enzymes, which, when secreted at hatching, break down the surrounding chorion in a one-off event [61]. Although little is known about the regulation of hatching gland enzyme release, secretion of this sort probably occurs by autophagosome/lysosome exocytosis, and several groups have shown that autophagy is linked to the secretion of lysosomal contents and secretory granules in specialized tissues [93,94]. It is therefore feasible that regulation of hatching gland enzyme release may require PI(3)P and PI(3)P binding proteins, which are downregulated in MZ-*fam83fa*$^{-/-}$ KO embryos, leading to the premature hatching phenotype we observe. This hypothesis, however, requires further experimental validation.

3.6. Fam83fa is targeted to the lysosome

The phenotypic manifestations we observed caused by loss of Fam83fa, namely accelerated hatching and an increased sensitivity to IR, could both be potentially explained by impaired autophagy as suggested by our RNA-seq data. As such, we next asked if Fam83fa is targeted to the lysosome. Previous work has shown that human and mouse FAM83F protein is targeted to the plasma membrane by a CAAX motif [23,25] and although zebrafish Fam83fa lacks a traditional CAAX motif, the

terminal amino acids are CIQS, where the invariant cysteine is predicted to be farnesylated in the same manner (GPS-Lipid 1.0 with high threshold parameters [54]). Following synthesis, many lysosomal membrane proteins, after transiting through the trans-Golgi network, are transported to the plasma membrane (reviewed in [95]). These proteins then subsequently travel to the lysosome via the endocytic pathway. To determine whether Fam8fa is also targeted to the lysosome, we expressed tandem fluorescently tagged Fam83fa protein (GFP, mCherry) in HEK293T cells. When overexpressed, a tandemly tagged protein of this sort normally appears yellow, but if it is targeted to the acidic condition of the lysosome, GFP fluorescence is quenched faster than that of mCherry, so puncta appear red [96]. Using confocal imaging of live cells, we confirmed that Fam83fa protein appears as red puncta, suggesting that Fam83fa is targeted to the lysosome (figure 6*a*). To confirm this conclusion, we treated cells with Bafilomycin A1 to inhibit acidification of the lysosome [97]. As expected, puncta were now yellow (figure 6*a,b*).

Many autophagy adaptors and receptors contain microtubule-associated proteins 1A/1B light chain 3B (hereafter referred to as LC3) interacting region (LIR) motifs that promote their recruitment by ATG8 subfamily proteins to the lysosome, where they are subsequently degraded [98]. Using iLIR, an *in silico* identifier of functional LIR motifs [99], we identified the LIR motif DTFEFI at position 503–508 of Fam83fa. If Fam83fa protein is targeted to the lysosome for degradation upon translation as our data suggest, then this may explain why, even when overexpressed, it can be hard to detect. Western blotting experiments performed in our laboratory previously detected substantially more Fam83fa protein when the C′ terminal amino acids, including the predicted LIR motif, were removed (electronic supplementary material, figure S1E). To test this hypothesis, we overexpressed tandem fluorescently tagged truncated Fam83fa protein (Fam83fa$^{1\text{-}500}$) in HEK293T cells and saw complete loss of puncta, indicating that deletion of the terminal 55 amino acids of Fam83fa leads to loss of lysosomal targeting (figure 6*a,b*). To confirm the interaction between the predicted LIR motif of Fam83fa and LC3 proteins, we attempted to run co-IP experiments. However, we were unable to express sufficient levels of the zebrafish LC3 proteins (Atg8 and Gabarap) to complete these experiments. Further work is therefore required to validate this interaction.

4. Discussion

Here, we explore the function of FAM83F in the zebrafish embryo. We show that *fam83fa* is strongly expressed in the hatching gland and that MZ-*fam83fa*$^{-/-}$ KO embryos hatch earlier than their WT counterparts. We also observe that MZ-*fam83fa*$^{-/-}$ embryos are more susceptible to IR than are their WT counterparts.

In attempting to understand these results, we first noted that Fam83fa has previously been reported to stabilize p53 [26]. This observation suggests that loss of Fam83fa should cause a decrease in levels of p53, and hence a reduction in IR-induced cell death—in other words, that embryos should be less susceptible to IR rather than more so, as demonstrated by *p53*$^{-/-}$ null zebrafish [77]. Our unexpected result suggested that levels of p53 might not be affected in MZ-*fam83fa*$^{-/-}$ embryos, and we confirmed this by western blotting—there were no differences in p53 levels between KO and WT embryos, whether or not they were treated with IR. Our conclusion differs from that of Salama *et al*. [26], although like them we noticed that overexpression of Fam83f in the zebrafish embryo does stabilize p53 and does cause an increase in p53-mediated gene transcription and apoptotic cell death (data not shown).

With p53 unlikely to be involved directly in the Fam83f mutant phenotype, we turned to RNA-seq to compare the transcriptomes of MZ-*fam83fa*$^{-/-}$ KO and WT embryos. Our results show that the genes most significantly downregulated in MZ-*fam83fa*$^{-/-}$ mutants encode putative PI(3)P binding proteins. PI(3)P and its associated proteins play important roles in autophagy [89,100,101], the process by which unneeded cytoplasmic material is degraded and recycled via proteolytic enzymes in the lysosome. Significantly, autophagy is activated (via p53) by IR (reviewed in [102]), and it can protect cells from apoptosis [103–106]. It is possible, therefore, that the downregulation of genes encoding PI(3)P binding proteins in MZ-*fam83fa*$^{-/-}$ mutants impairs autophagy and make cells more susceptible to apoptosis.

Autophagy involves the secretion of lysosomal contents and the release of secretory granules [93,94]. Further evidence that Fam83f might be associated with autophagy comes from our observation that this protein is targeted to the lysosome (figure 6*a,b*), which is dependent upon a signal sequence in the terminal 55 amino acids that is predicted to contain a lysosome-targeting LIR motif. Furthermore, human FAM83F interacts with syntaxins 7 and 8 (G.S. 2024, unpublished data), which are important in late endosome–lysosome fusion [107] and the vesicle-associated membrane protein 8 (VAMP8), which is associated with the exocytosis of secretory organelles [108].

What of the premature hatching of MZ-*fam83fa*$^{-/-}$ embryos? Hatching gland cells contain large, lysosome-like granules of proteolytic enzymes, which, when secreted, break down the surrounding chorion in a one-off event that corresponds with hatching [61]. Little is known about how this process is timed, but the high levels of expression of *fam83fa* in the hatching gland, and the localization of the protein to the lysosome, suggest that Fam83fa may be involved in some way, and that temporal regulation of hatching gland enzyme release is disrupted in MZ-*fam83fa*$^{-/-}$ KO embryos. Several groups have shown that autophagy is linked to the secretion of lysosomal contents in specialized tissues (such as the hatching gland) and that this probably occurs through autophagosome exocytosis [93,94]. Intuitively therefore, loss of the autophagy-related, lysosomal protein Fam83fa, could have a significant impact on the temporal release of lysosomal contents such as hatching gland enzymes.

This is a subject for further study, together with investigating the relationship between Fam83fa and PI(3)P binding proteins.

A key limitation of this work is the inability to undertake a rescue experiment in which *fam83fa* mRNA is injected into MZ-*fam83fa*$^{-/-}$ KO zebrafish embryos to attempt to rescue the hatching and/or genotoxic sensitivity phenotypes. Such experiments would provide valuable confirmation that the observed phenotypes are caused by loss of Fam83fa. However, as injection of *fam83fa* mRNA has been shown to induce the DDR as an overexpression phenotype ([26] and data not shown), it would be near impossible to unpick a rescued phenotype from an overexpression phenotype, particularly given the low level of baseline

expression of *fam83fa* to begin with. We consider the use of two different genetic KO zebrafish lines, that both show the same phenotype, to be sufficient evidence of the role of Fam83f *in vivo*, in the absence of a specific rescue experiment.

Using zebrafish as a model, we have uncovered a previously unappreciated role for Fam83f in both embryonic hatching and sensitivity to DNA damage, the in-depth mechanisms of which are now open questions for investigation. This descriptive work provides a deeper understanding of the role that Fam83f plays *in vivo*, contributing not only to our understanding of early development but also to the pathology of human disease, given the prevalence of FAM83F dysregulation and misexpression in several human cancers.

Ethics. All animal work, including housing and husbandry, was undertaken in accordance with the Crick Use of Animals in Research Policy, the Animals (Scientific Procedures) Act 1986 (ASPA) implemented by the Home Office in the UK and the Animal Welfare Act 2006. Consideration was given to the 3R's in experimental design. All regulated procedures were carried out at the Francis Crick Institute in accordance with UK Home Office regulations under project license PF59163DB, which underwent full ethical review and approval by the Francis Crick Institute's Animal Ethics Committee.

Data accessibility. RNA-seq data published in this report are accessible through GEO Series accession number GSE244291 (https://www.ncbi.nlm.nih.gov/geo/query/acc.cgi?acc=GSE244291). Plasmid DNA sequences can be accessed at Genbank accession PQ064475.

Supplementary material is available online [109].

Declaration of AI use. We have not used AI-assisted technologies in creating this article.

Authors' contributions. R.A.J.: conceptualization, data curation, formal analysis, investigation, methodology, visualization, writing—original draft; F.C.: data curation, formal analysis, investigation, methodology, writing—review and editing; G.K.: formal analysis, visualization, writing—review and editing; D.B.: methodology, software, writing—review and editing; M.J.R.: data curation, visualization, writing—review and editing; G.S.: conceptualization, investigation, writing—review and editing; J.C.S.: conceptualization, funding acquisition, project administration, supervision, writing—review and editing.

All authors gave final approval for publication and agreed to be held accountable for the work performed therein.

Conflict of interest declaration. We declare we have no competing interests.

Funding. This work was supported by the Francis Crick Institute, which receives its core funding from Cancer Research UK (FC001–157), the UK Medical Research Council (FC001–157) and the Wellcome Trust (FC001–157).

Acknowledgements. The authors thank Mollie Millington, Sarah Wheatley and all of the Francis Crick Institute Aquatics team for their invaluable help and patience. We thank the Francis Crick Advanced Light Microscopy Science Technology Platform (STP), the Scientific Computing STP, Dr Robert Goldstone of the Advanced Sequencing Facility (ASF) STP and Dr Nourdine Bah of the Bioinformatics and Biostatistics STP. We thank Drs Karen Vousden and Robert Ludwig (The Francis Crick Institute) for invaluable advice on the DNA damage response and Dr Sharon Tooze (The Francis Crick Institute) for autophagy advice and reagents. Finally, we thank Dr Karen Dunbar and the Sapkota lab (University of Dundee) for a most enjoyable collaboration, and members of the Smith lab for helpful discussion.

References

1. Bartel CA, Parameswaran N, Cipriano R, Jackson MW. 2016 FAM83 proteins: Fostering new interactions to drive oncogenic signaling and therapeutic resistance. *Oncotarget* **7**, 52597–52612. (doi:10.18632/oncotarget.9544)
2. Zerbino DR *et al*. 2018 Ensembl 2018. *Nucleic Acids Res*. **46**, D754–D761. (doi:10.1093/nar/gkx1098)
3. Bozatzi P *et al*. 2018 PAWS1 controls Wnt signalling through association with casein kinase 1α. *EMBO Rep.* **19**, e44807. (doi:10.15252/embr.201744807)
4. Madej T, Lanczycki CJ, Zhang D, Thiessen PA, Geer RC, Marchler-Bauer A, Bryant SH. 2014 MMDB and VAST+: tracking structural similarities between macromolecular complexes. *Nucleic Acids Res*. **42**, D297–303. (doi:10.1093/nar/gkt1208)
5. Cipriano R, Graham J, Miskimen KLS, Bryson BL, Bruntz RC, Scott SA, Brown HA, Stark GR, Jackson MW. 2012 FAM83B mediates EGFR- and RAS-driven oncogenic transformation. *J. Clin. Invest*. **122**, 3197–3210. (doi:10.1172/JCI60517)
6. Lee SY, Meier R, Furuta S, Lenburg ME, Kenny PA, Xu R, Bissell MJ. 2012 FAM83A confers EGFR-TKI resistance in breast cancer cells and in mice. *J. Clin. Invest*. **122**, 3211–3220. (doi:10.1172/JCI60498)
7. Mao Y, Liu J, Zhang D, Li B. 2016 miR-143 inhibits tumor progression by targeting FAM83F in esophageal squamous cell carcinoma. *Tumor Biol*. **37**, 9009–9022. (doi:10.1007/s13277-015-4760-9)
8. Fuziwara CS, Saito KC, Leoni SG, Waitzberg ÂFL, Kimura ET. 2019 The highly expressed FAM83F protein in papillary thyroid cancer exerts a pro-oncogenic role in thyroid follicular cells. *Front. Endocrinol.***10**, 134. (doi:10.3389/fendo.2019.00134)
9. Gu GM, Zhan YY, Abuduwaili K, Wang XL, Li XQ, Zhu HG, Liu CL. 2018 MiR-940 inhibits the progression of NSCLC by targeting FAM83F. *Eur. Rev. Med. Pharmacol. Sci.* **22**, 5964–5971. (doi:10.26355/eurrev_201809_15927)
10. Fang K, Chen X, Qiu F, Xu J, Xiong H, Zhang Z. 2022 Serum-derived exosomes-mediated circular rna arhgap10 modulates the progression of non-small cell lung cancer through the mir-638/fam83f axis. *Cancer Biother. Radiopharm*. **37**, 96–110. (doi:10.1089/cbr.2019.3534)
11. Gan J, Li Y, Meng Q. 2020 Systematic analysis of expression profiles and prognostic significance for *FAM83* family in non-small-cell lung cancer. *Front. Mol. Biosci*. **7**, 572406. (doi:10.3389/fmolb.2020.572406)
12. Zhang C *et al*. 2023 Upregulation of FAM83F by c-Myc promotes cervical cancer growth and aerobic glycolysis via Wnt/β-catenin signaling activation. *Cell Death Dis*. **14**, 837. (doi:10.1038/s41419-023-06377-9)
13. Jin Y, Yu J, Jiang Y, Bu J, Zhu T, Gu X, Zhu X. 2022 Comprehensive analysis of the expression, prognostic significance, and function of FAM83 family members in breast cancer. *World J. Surg. Oncol*. **20**, 1–18. (doi:10.1186/s12957-022-02636-9)
14. Snijders AM, Lee SY, Hang B, Hao W, Bissell MJ, Mao JH. 2017 FAM83 family oncogenes are broadly involved in human cancers: an integrative multi-omics approach. *Mol. Oncol*. **11**, 167–179. (doi:10.1002/1878-0261.12016)
15. Jiang Y, Yu J, Zhu T, Bu J, Hu Y, Liu Y, Zhu X, Gu X. 2023 Involvement of FAM83 family proteins in the development of solid tumors: an update review. *J. Cancer* **14**, 1888–1903. (doi:10.7150/jca.83420)

16. Yuan S *et al*. 2022 Pan-cancer analysis of the FAM83 family and its association with prognosis and tumor microenvironment. *Front. Genet.* **13**, 919559. (doi:10.3389/fgene.2022.919559)
17. Cipriano R, Miskimen KLS, Bryson BL, Foy CR, Bartel CA, Jackson MW. 2013 FAM83B-mediated activation of PI3K/AKT and MAPK signaling cooperates to promote epithelial cell transformation and resistance to targeted therapies. *Oncotarget* **4**, 729–738. (doi:10.18632/oncotarget.1027)
18. Santamaria A, Nagel S, Sillje HHW, Nigg EA. 2008 The spindle protein chica mediates localization of the chromokinesin kid to the mitotic spindle. *Curr. Biol*. **18**, 723–729. (doi:10.1016/j.cub.2008.04.041)
19. Dunsch AK, Hammond D, Lloyd J, Schermelleh L, Gruneberg U, Barr FA. 2012 Dynein light chain 1 and a spindle-associated adaptor promote dynein asymmetry and spindle orientation. *J. Cell Biol*. **198**, 1039–1054. (doi:10.1083/jcb.201202112)
20. Vogt J, Dingwell KS, Herhaus L, Gourlay R, Macartney T, Campbell D, Smith JC, Sapkota GP. 2014 Protein associated with SMAD1 (PAWS1/FAM83G) is a substrate for type I bone morphogenetic protein receptors and modulates bone morphogenetic protein signalling. *Open Biol*. **4**, 130210. (doi:10.1098/rsob.130210)
21. Cummins TD *et al*. 2017 FAM83G/PAWS1 controls cytoskeletal dynamics and cell migration through association with the SH3 adaptor CD2AP. *Cell Biology*. (doi:10.1101/106971)
22. Kuga T *et al*. 2016 FAM83H and casein kinase I regulate the organization of the keratin cytoskeleton and formation of desmosomes. *Sci. Rep*. **6**, 26557. (doi:10.1038/srep26557)
23. Fulcher LJ *et al*. 2018 The DUF1669 domain of FAM83 family proteins anchor casein kinase 1 isoforms. *Sci. Signal*. **11**, eaao2341. (doi:10.1126/scisignal.aao2341)
24. Knippschild U, Krüger M, Richter J, Xu P, García-Reyes B, Peifer C, Halekotte J, Bakulev V, Bischof J. 2014 The CK1 family: contribution to cellular stress response and its role in carcinogenesis. *Front. Oncol*. **4**, 96. (doi:10.3389/fonc.2014.00096)
25. Dunbar K, Jones RA, Dingwell K, Macartney TJ, Smith JC, Sapkota GP. 2020 FAM83F regulates canonical wnt signalling through an interaction with CK1α. *Cell Biol.*. (doi:10.1101/2020.05.25.114504)
26. Salama M *et al*. 2019 Fam83F induces p53 stabilisation and promotes its activity. *Cell Death Differ*. **26**, 2125–2138. (doi:10.1038/s41418-019-0281-1)
27. Zhang P, Kratz AS, Salama M, Elabd S, Heinrich T, Wittbrodt J, Blattner C, Davidson G. 2015 Expression screening using a Medaka cDNA library identifies evolutionarily conserved regulators of the p53/Mdm2 pathway. *BMC Biotechnol*. **15**, 92. (doi:10.1186/s12896-015-0208-y)
28. Pandey AK, Lu L, Wang X, Homayouni R, Williams RW. 2014 Functionally enigmatic genes: a case study of the brain ignorome. *PLoS One* **9**, e88889. (doi:10.1371/journal.pone.0088889)
29. Stoeger T, Gerlach M, Morimoto RI, Nunes Amaral LA. 2018 Large-scale investigation of the reasons why potentially important genes are ignored. *PLoS Biol.* **16**, e2006643. (doi:10.1371/journal.pbio.2006643)
30. Faber J, Nieuwkoop PD. 2020 *Normal table of Xenopus laevis (Daudin): a systematical & chronological survey of the development from the fertilized egg till the end of metamorphosis*. New York, NY: Garland Science.
31. Slack JMW. 1984 Regional biosynthetic markers in the early amphibian embryo. *Development* **80**, 289–319. (doi:10.1242/dev.80.1.289)
32. Montague TG, Cruz JM, Gagnon JA, Church GM, Valen E. 2014 CHOPCHOP: a CRISPR/Cas9 and TALEN web tool for genome editing. *Nucleic Acids Res*. **42**, W401–7. (doi:10.1093/nar/gku410)
33. Burger A *et al*. 2016 Maximizing mutagenesis with solubilized CRISPR-Cas9 ribonucleoprotein complexes. *Development* (doi:10.1242/dev.134809)
34. Gagnon JA *et al*. 2014 Efficient mutagenesis by Cas9 protein-mediated oligonucleotide insertion and large-scale assessment of single-guide RNAs. *PLoS One* **9**, e98186. (doi:10.1371/journal.pone.0098186)
35. Hwang WY, Fu Y, Reyon D, Maeder ML, Tsai SQ, Sander JD, Peterson RT, Yeh JRJ, Joung JK. 2013 Efficient genome editing in zebrafish using a CRISPR-Cas system. *Nat. Biotechnol*. **31**, 227–229. (doi:10.1038/nbt.2501)
36. Rouet R, de Oñate L, Li J, Murthy N, Wilson RC. 2018 Engineering CRISPR-Cas9 RNA-protein complexes for improved function and delivery. *CRISPR J.* **1**, 367–378. (doi:10.1089/crispr.2018.0037)
37. Conant D *et al*. 2022 Inference of CRISPR edits from Sanger trace data. *CRISPR J.* **5**. (doi:10.1089/crispr.2021.0113)
38. Tanaka S, Yoshioka S, Nishida K, Hosokawa H, Kakizuka A, Maegawa S. 2018 *In vivo* targeted single-nucleotide editing in zebrafish. *Sci. Rep*. **8**, 11423. (doi:10.1038/s41598-018-29794-9)
39. Agrotis A, Ketteler R. 2015 A new age in functional genomics using CRISPR/Cas9 in arrayed library screening. *Front. Genet.* **6**, 300. (doi:10.3389/fgene.2015.00300)
40. Thisse C, Thisse B. 2008 High-resolution *in situ* hybridization to whole-mount zebrafish embryos. *Nat. Protoc*. **3**, 59–69. (doi:10.1038/nprot.2007.514)
41. Schindelin J *et al*. 2012 Fiji: an open-source platform for biological-image analysis. *Nat. Methods* **9**, 676–682. (doi:10.1038/nmeth.2019)
42. Rossner M, Yamada KM. 2004 What's in a picture? The temptation of image manipulation. *J. Cell Biol*. **166**, 11–15. (doi:10.1083/jcb.200406019)
43. Edelstein AD, Tsuchida MA, Amodaj N, Pinkard H, Vale RD, Stuurman N. 2014 Advanced methods of microscope control using μmanager software. *J. Biol. Methods* **1**, 10. (doi:10.14440/jbm.2014.36)
44. Jones RA, Renshaw MJ, Barry DJ, Smith JC. 2022 Automated staging of zebrafish embryos using machine learning. *Wellcome Open Res*. **7**, 275. (doi:10.12688/wellcomeopenres.18313.3)
45. Edgar R, Domrachev M, Lash AE. 2002 Gene expression omnibus: NCBI gene expression and hybridization array data repository. *Nucleic Acids Res*. **30**, 207–210. (doi:10.1093/nar/30.1.207)
46. Barrett T *et al*. 2012 NCBI GEO: archive for functional genomics data sets—update. *Nucleic Acids Res*. **41**, D991–D995. (doi:10.1093/nar/gks1193)
47. BABS-STP. 2023 BABS-STP/js608: Scripts for publication (Version v1). Zenodo (doi:10.5281/zenodo.10423384)
48. Untergasser A, Cutcutache I, Koressaar T, Ye J, Faircloth BC, Remm M, Rozen SG. 2012 Primer3—new capabilities and interfaces. *Nucleic Acids Res*. **40**, e115–e115. (doi:10.1093/nar/gks596)
49. Livak KJ, Schmittgen TD. 2001 Analysis of relative gene expression data using real-time quantitative PCR and the 2−ΔΔCT method. *Methods* **25**, 402–408. (doi:10.1006/meth.2001.1262)
50. Bustin SA *et al*. 2009 The MIQE guidelines: minimum information for publication of quantitative real-time PCR experiments. *Clin. Chem*. **55**, 611–622. (doi:10.1373/clinchem.2008.112797)
51. Lee KC *et al*. 2008 Detection of the p53 response in zebrafish embryos using new monoclonal antibodies. *Oncogene* **27**, 629–640. (doi:10.1038/sj.onc.1210695)
52. Glasauer SMK, Neuhauss SCF. 2014 Whole-genome duplication in teleost fishes and its evolutionary consequences. *Mol. Genet. Genomics* **289**, 1045–1060. (doi:10.1007/s00438-014-0889-2)
53. Hancock JF, Cadwallader K, Paterson H, Marshall CJ. 1991 A CAAX or A CAAL motif and a second signal are sufficient for plasma membrane targeting of ras proteins. *EMBO J.* **10**, 4033–4039. (doi:10.1002/j.1460-2075.1991.tb04979.x)
54. Xie Y *et al*. 2016 GPS-Lipid: a robust tool for the prediction of multiple lipid modification sites. *Sci. Rep.* **6**, 28249. (doi:10.1038/srep28249)

55. White RJ *et al*. 2017 A high-resolution mRNA expression time course of embryonic development in zebrafish. *eLife* **6**, e30860. (doi:10.7554/eLife.30860)
56. Kimmel CB, Ballard WW, Kimmel SR, Ullmann B, Schilling TF. 1995 Stages of embryonic development of the zebrafish. *Dev. Dyn*. **203**, 253–310. (doi:10.1002/aja.1002030302)
57. Wang H, Holland PWH, Takahashi T. 2019 Gene profiling of head mesoderm in early zebrafish development: insights into the evolution of cranial mesoderm. *Evodevo* **10**, 14. (doi:10.1186/s13227-019-0128-3)
58. Musen MA, Noy NF, Shah NH, Whetzel PL, Chute CG, Story MA, Smith B. 2012 The National Center for Biomedical Ontology. *J. Am. Med. Inform. Assoc.* **19**, 190–195. (doi:10.1136/amiajnl-2011-000523)
59. Martínez-romero RM, Jonquet C, O'connor O, Graybeal J, PAZOS A, MUSEN MA. 2017 NCBO ontology recommender 2.0: an enhanced approach for biomedical ontology recommendation. *J. Biomed. Semantics* **8**, 21. (doi:10.1186/s13326-017-0128-y)
60. Whetzel PL, Noy NF, Shah NH, Alexander PR, Nyulas C, Tudorache T, Musen MA. 2011 BioPortal: enhanced functionality via new web services from the national center for biomedical ontology to access and use ontologies in software applications. *Nucleic Acids Res*. **39**, W541–5. (doi:10.1093/nar/gkr469)
61. Trikić MZ, Monk P, Roehl H, Partridge LJ. 2011 Regulation of zebrafish hatching by tetraspanin cd63. *PLoS One* **6**, e19683. (doi:10.1371/journal.pone.0019683)
62. Nagasawa T, Kawaguchi M, Yano T, Sano K, Okabe M, Yasumasu S. 2016 Evolutionary changes in the developmental origin of hatching gland cells in basal ray-finned fishes. *Zool. Sci.* **33**, 272. (doi:10.2108/zs150183)
63. Vogel AM, Gerster T. 1997 Expression of a zebrafish Cathepsin L gene in anterior mesendoderm and hatching gland. *Dev. Genes Evol*. **206**, 477–479. (doi:10.1007/s004270050078)
64. Parichy DM, Elizondo MR, Mills MG, Gordon TN, Engeszer RE. 2009 Normal table of postembryonic zebrafish development: staging by externally visible anatomy of the living fish. *Dev. Dyn.* **238**, 2975–3015. (doi:10.1002/dvdy.22113)
65. Gardiner MR, Daggett DF, Zon LI, Perkins AC. 2005 Zebrafish *KLF4* is essential for anterior mesendoderm/pre-polster differentiation and hatching . *Dev. Dyn*. **234**, 992–996. (doi:10.1002/dvdy.20571)
66. Blanco MJ, Barrallo-Gimeno A, Acloque H, Reyes AE, Tada M, Allende ML, Mayor R, Nieto MA. 2007 Snail1a and Snail1b cooperate in the anterior migration of the axial mesendoderm in the zebrafish embryo. *Development* **134**, 4073–4081. (doi:10.1242/dev.006858)
67. Wagner A. 1996 Genetic redundancy caused by gene duplications and its evolution in networks of transcriptional regulators. *Biol. Cybern*. **74**, 557–567. (doi:10.1007/BF00209427)
68. Rossi A, Kontarakis Z, Gerri C, Nolte H, Hölper S, Krüger M, Stainier DYR. 2015 Genetic compensation induced by deleterious mutations but not gene knockdowns. *Nature* **524**, 230–233. (doi:10.1038/nature14580)
69. El-Brolosy MA *et al*. 2019 Genetic compensation triggered by mutant mRNA degradation. *Nature* **568**, 193–197. (doi:10.1038/s41586-019-1064-z)
70. Hug N, Longman D, Cáceres JF. 2016 Mechanism and regulation of the nonsense-mediated decay pathway. *Nucleic Acids Res*. **44**, 1483–1495. (doi:10.1093/nar/gkw010)
71. Cotelli F, Andronico F, Brivio M, Lamia CL. 1988 Structure and composition of the fish egg chorion (*Carassius auratus*). *J. Ultrastruct. Mol. Struct. Res*. **99**, 70–78. (doi:10.1016/0889-1605(88)90034-1)
72. Ninness MM, Stevens ED, Wright PA. 2006 Removal of the chorion before hatching results in increased movement and accelerated growth in rainbow trout (*Oncorhynchus mykiss*) embryos. *J. Exp. Biol.* **209**, 1874–1882. (doi:10.1242/jeb.02200)
73. White JK *et al*. 2013 Genome-wide generation and systematic phenotyping of knockout mice reveals new roles for many genes. *Cell* **154**, 452–464. (doi:10.1016/j.cell.2013.06.022)
74. Barbaric I, Miller G, Dear TN. 2007 Appearances can be deceiving: phenotypes of knockout mice. *Brief. Funct. Genom. Proteom*. **6**, 91–103. (doi:10.1093/bfgp/elm008)
75. Minchin JEN, Scahill CM, Staudt N, Busch-Nentwich EM, Rawls JF. 2018 Deep phenotyping in zebrafish reveals genetic and diet-induced adiposity changes that may inform disease risk. *J. Lipid Res*. **59**, 1536–1545. (doi:10.1194/jlr.D084525)
76. Allalou A, Wu Y, Ghannad-Rezaie M, Eimon PM, Yanik MF. 2017 Automated deep-phenotyping of the vertebrate brain. *eLife* **6**, e23379. (doi:10.7554/eLife.23379)
77. Elabd S, Jabeen NA, Gerber V, Peravali R, Bourdon JC, Kancherla S, Vallone D, Blattner C. 2019 Delay in development and behavioural abnormalities in the absence of p53 in zebrafish. *PLoS One* **14**, e0220069. (doi:10.1371/journal.pone.0220069)
78. Danilova N *et al*. 2014 The role of DNA damage response in zebrafish and cellular models of diamond blackfan anemia. *Dis. Model. Mech*. (doi:10.1242/dmm.015495)
79. Sirbu BM, Cortez D. 2013 DNA damage response: three levels of DNA repair regulation. *Cold Spring Harb. Perspect. Biol.* **5**, a012724. (doi:10.1101/cshperspect.a012724)
80. Love MI, Huber W, Anders S. 2014 Moderated estimation of fold change and dispersion for RNA-seq data with DESeq2. *Genome Biol.* **15**, 550. (doi:10.1186/s13059-014-0550-8)
81. Tsuji S, Yamashita M, Hoffman DR, Nishiyama A, Shinohara T, Ohtsu T, Shibata Y. 2009 Capture of heat-killed *Mycobacterium bovis* bacillus Calmette-guérin by intelectin-1 deposited on cell surfaces. *Glycobiology* **19**, 518–526. (doi:10.1093/glycob/cwp013)
82. Ding Z, Zhao X, Wang J, Zhang F, Wang W, Liu H. 2019 Intelectin mediated phagocytosis and killing activity of macrophages in blunt snout bream (*Megalobrama amblycephala*). *Fish Shellfish Immunol*. **87**, 129–135. (doi:10.1016/j.fsi.2019.01.001)
83. Bradford YM *et al*. 2022 Zebrafish information network, the knowledgebase for danio rerio research. *Genetics* **220**, iyac016. (doi:10.1093/genetics/iyac016)
84. Yilmaz O, Patinote A, Com E, Pineau C, Bobe J. 2021 Knock out of specific maternal vitellogenins in zebrafish (Danio rerio) evokes vital changes in egg proteomic profiles that resemble the phenotype of poor quality eggs. *BMC Genomics* **22**, 308.
85. Mabin JW, Woodward LA, Patton RD, Yi Z, Jia M, Wysocki VH, Bundschuh R, Singh G. 2018 The exon junction complex undergoes a compositional switch that alters mRNP structure and nonsense-mediated mRNA decay activity. *Cell Rep.* **25**, 2431–2446. (doi:10.1016/j.celrep.2018.11.046)
86. Stinchi S, Lullmann-Rauch R, Hartmann D, Coenen R, Beccari T, Orlacchio A, von Figura K, Saftig P. 1999 Targeted disruption of the lysosomal-mannosidase gene results in mice resembling a mild form of human mannosidosis. *Hum. Mol. Genet*. **8**, 1365–1372. (doi:10.1093/hmg/8.8.1365)
87. Yoshii SR, Mizushima N. 2017 Monitoring and measuring autophagy. *Int. J. Mol. Sci.* **18**, 1865. (doi:10.3390/ijms18091865)
88. Edgar R, Domrachev M, Lash AE. 2002 Gene Expression Omnibus: NCBI gene expression and hybridization array data repository. *Nucleic Acids Res.* **30**, 207–210.
89. Palamiuc L, Ravi A, Emerling BM. 2020 Phosphoinositides in autophagy: current roles and future insights. *FEBS J.* **287**, 222–238. (doi:10.1111/febs.15127)
90. Li L *et al*. 2021 Lipids and membrane-associated proteins in autophagy. *Protein Cell* **12**, 520–544. (doi:10.1007/s13238-020-00793-9)
91. Czarny P, Pawlowska E, Bialkowska-Warzecha J, Kaarniranta K, Blasiak J. 2015 Autophagy in DNA damage response. *Int. J. Mol. Sci.* **16**, 2641–2662. (doi:10.3390/ijms16022641)
92. Levy JMM, Towers CG, Thorburn A. 2017 Targeting autophagy in cancer. *Nat. Rev. Cancer* **17**, 528–542. (doi:10.1038/nrc.2017.53)
93. Cadwell K *et al*. 2008 A key role for autophagy and the autophagy gene Atg16l1 in mouse and human intestinal paneth cells. *Nature* **456**, 259–263. (doi:10.1038/nature07416)
94. DeSelm CJ *et al*. 2011 Autophagy proteins regulate the secretory component of osteoclastic bone resorption. *Dev. Cell* **21**, 966–974. (doi:10.1016/j.devcel.2011.08.016)
95. Saftig P, Klumperman J. 2009 Lysosome biogenesis and lysosomal membrane proteins: trafficking meets function. *Nat. Rev. Mol. Cell Biol*. **10**, 623–635. (doi:10.1038/nrm2745)
96. Kimura S, Noda T, Yoshimori T. 2007 Dissection of the autophagosome maturation process by a novel reporter protein, tandem fluorescent-tagged LC_3. *Autophagy* **3**, 452–460. (doi:10.4161/auto.4451)

97. Gagliardi S, Gatti PA, Belfiore P, Zocchetti A, Clarke GD, Farina C. 1998 Synthesis and structure-activity relationships of bafilomycin A1 derivatives as inhibitors of vacuolar H+-ATPase. *J. Med. Chem.* **41**, 1883–1893. (doi:10.1021/jm9707838)
98. Wirth M, Zhang W, Razi M, Nyoni L, Joshi D, O'Reilly N, Johansen T, Tooze SA, Mouilleron S. 2019 Molecular determinants regulating selective binding of autophagy adapters and receptors to ATG8 proteins. *Nat. Commun*. **10**, 2055. (doi:10.1038/s41467-019-10059-6)
99. Kalvari I, Tsompanis S, Mulakkal NC, Osgood R, Johansen T, Nezis IP, Promponas VJ. 2014 iLIR: a web resource for prediction of Atg8-family interacting proteins. *Autophagy* **10**, 913–925. (doi:10.4161/auto.28260)
100. Nishimura T, Tooze SA. 2020 Emerging roles of ATG proteins and membrane lipids in autophagosome formation. *Cell Discov.* **6**, 32. (doi:10.1038/s41421-020-0161-3)
101. Dall'Armi C, Devereaux KA, Di Paolo G. 2013 The role of lipids in the control of autophagy. *Curr. Biol.* **23**, R33–45. (doi:10.1016/j.cub.2012.10.041)
102. White E. 2016 Autophagy and p53. *Cold Spring Harb. Perspect. Med*. **6**, a026120. (doi:10.1101/cshperspect.a026120)
103. Abedin MJ, Wang D, McDonnell MA, Lehmann U, Kelekar A. 2007 Autophagy delays apoptotic death in breast cancer cells following DNA damage. *Cell Death Differ*. **14**, 500–510. (doi:10.1038/sj.cdd.4402039)
104. Muñoz-Gámez JA *et al*. 2009 PARP-1 is involved in autophagy induced by DNA damage. *Autophagy* **5**, 61–74. (doi:10.4161/auto.5.1.7272)
105. Huang Q, Shen HM. 2009 To die or to live: the dual role of poly (ADP-ribose) polymerase-1 in autophagy and necrosis under oxidative stress and DNA damage. *Autophagy* **5**, 273–276. (doi:10.4161/auto.5.2.7640)
106. Vessoni AT, Filippi-Chiela EC, Menck CF, Lenz G. 2013 Autophagy and genomic integrity. *Cell Death Differ*. **20**, 1444–1454. (doi:10.1038/cdd.2013.103)
107. Pryor PR *et al*. 2004 Combinatorial SNARE complexes with VAMP7 or VAMP8 define different late endocytic fusion events. *EMBO Rep*. **5**, 590–595. (doi:10.1038/sj.embor.7400150)
108. Loo LS, Hwang L, Ong YM, Tay HS, Wang C, Hong W. 2009 A role for endobrevin/VAMP8 in CTL lytic granule exocytosis. *Eur. J. Immunol*. **39**, 3520–3528. (doi:10.1002/eji.200939378)
109. Jones RA, Cooper F, Kelly G, Barry D, Renshaw MJ, Gopal S *et al*. 2024 Supplementary material from: Zebrafish reveal new roles for Fam83f in hatching and the DNA damage-mediated autophagic response. FigShare (doi:10.6084/m9.figshare.c.7468066)